The Astrophysical Journal, 951:119 (20pp), 2023 July 10 https://doi.org/10.3847/1538-4357/acd341
© 2023. The Author(s). Published by the American Astronomical Society.
OPEN ACCESS

ODIN: Where Do Lyα Blobs Live? Contextualizing Blob Environments within Large-scale Structure

Vandana Ramakrishnan[1], Byeongha Moon[2], Sang Hyeok Im[3], Rameen Farooq[4], Kyoung-Soo Lee[1], Eric Gawiser[4], Yujin Yang[2], Changbom Park[5], Ho Seong Hwang[3,6], Francisco Valdes[7], Maria Celeste Artale[1,8,9,10], Robin Ciardullo[11,12], Arjun Dey[13], Caryl Gronwall[11,12], Lucia Guaita[10], Woong-Seob Jeong[2], Nelson Padilla[14], Akriti Singh[10], and Ann Zabludoff[15]

[1] Department of Physics and Astronomy, Purdue University, 525 Northwestern Avenue, West Lafayette, IN 47907, USA; ramakr18@purdue.edu
[2] Korea Astronomy and Space Science Institute, 776 Daedeokdae-ro, Yuseong-gu, Daejeon 34055, Republic of Korea
[3] Department of Physics and Astronomy, Seoul National University, 1 Gwanak-ro, Gwanak-gu, Seoul 08826, Republic of Korea
[4] Physics and Astronomy Department, Rutgers, The State University, Piscataway, NJ 08854, USA
[5] Korea Institute for Advanced Study, 85 Hoegi-ro, Dongdaemun-gu, Seoul 02455, Republic of Korea
[6] SNU Astronomy Research Center, Seoul National University, 1 Gwanak-ro, Gwanak-gu, Seoul 08826, Republic of Korea
[7] National Optical Astronomy Observatory, 950 N. Cherry Avenue, Tucson, AZ 85719, USA
[8] Physics and Astronomy Department Galileo Galilei, University of Padova, Vicolo dell'Osservatorio 3, I-35122 Padova, Italy
[9] INFN–Padova, Via Marzolo 8, I-35131 Padova, Italy
[10] Departamento de Ciencias Fisicas, Universidad Andres Bello, Fernandez Concha 700, Las Condes, Santiago, Chile
[11] Department of Astronomy & Astrophysics, The Pennsylvania State University, University Park, PA 16802, USA
[12] Institute for Gravitation and the Cosmos, The Pennsylvania State University, University Park, PA 16802, USA
[13] NSF's National Optical-Infrared Astronomy Research Laboratory, 950 N. Cherry Avenue, Tucson, AZ 85719, USA
[14] Instituto de Astronomía Teórica y Experimental (IATE), Comisión Nacional de Investigaciones Científicas y Técnicas (CONICET), Universidad Nacional de Córdoba, Laprida 854, X500BGR Córdoba, Argentina
[15] Steward Observatory, University of Arizona, 933 N. Cherry Avenue, Tucson, AZ 85721, USA
Received 2023 February 10; revised 2023 April 18; accepted 2023 May 6; published 2023 July 7

Abstract

While many Lyα blobs (LABs) are found in and around several well-known protoclusters at high redshift, how they trace the underlying large-scale structure is still poorly understood. In this work, we utilize 5352 Lyα emitters (LAEs) and 129 LABs at $z = 3.1$ identified over a $\sim$9.5 deg^2 area in early data from the ongoing One-hundred-deg^2 DECam Imaging in Narrowbands (ODIN) survey to investigate this question. Using LAEs as tracers of the underlying matter distribution, we identify overdense structures as galaxy groups, protoclusters, and filaments of the cosmic web. We find that LABs preferentially reside in regions of higher-than-average density and are located in closer proximity to overdense structures, which represent the sites of protoclusters and their substructures. Moreover, protoclusters hosting one or more LABs tend to have a higher descendant mass than those which do not. Blobs are also strongly associated with filaments of the cosmic web, with $\sim$70% of the population being within a projected distance of $\sim$2.4 pMpc from a filament. We show that the proximity of LABs to protoclusters is naturally explained by their association with filaments as large cosmic structures are where many filaments converge. The contiguous wide-field coverage of the ODIN survey allows us to establish firmly a connection between LABs as a population and filaments of the cosmic web for the first time.

Unified Astronomy Thesaurus concepts: High-redshift galaxy clusters (2007); Galaxy clusters (584); Lyman-alpha galaxies (978)

1. Introduction

In the local universe, galaxies in overdense environments tend to be more massive (e.g., van der Burg et al. 2013) and are more likely to be quiescent (e.g., Peng et al. 2010; Quadri et al. 2012). At $z \gtrsim 1.5$, this trend weakens (Alberts et al. 2014, 2016; Nantais et al. 2016; Kawinwanichakij et al. 2017) or even reverses (Elbaz et al. 2007; Hwang et al. 2019; Lemaux et al. 2022). At $z \gtrsim 2$, the highest-density regions—believed to be the locations of the progenitors of present-day galaxy clusters, or protoclusters—display copious star formation and active galactic nucleus (AGN) activity, often in excess of those observed in regions of average density (e.g., Casey et al. 2015; Umehata et al. 2015; Oteo et al. 2018; Harikane et al. 2019; Shi et al. 2020). To gain insight into how the large-scale environment influences the evolution of galaxies over cosmic time, it is necessary to study a large sample of overdense structures at high redshift and the galaxy inhabitants therein.

Lacking many of the observable markers of fully virialized clusters, protoclusters are often identified as overdensities of galaxies such as dusty star-forming galaxies (Oteo et al. 2018), Lyman break galaxies (e.g., Toshikawa et al. 2016, 2018), Hα emitters (e.g., Hayashi & Kodama 2012; Darvish et al. 2020; Koyama et al. 2021), or Lyα emitters (LAEs; e.g., Lee et al. 2014; Jiang et al. 2018; Harikane et al. 2019; Higuchi et al. 2019). Alternatively, several "signposts" have been explored as promising avenues to find them. These include radio galaxies and QSOs, and more recently, Lyα nebulae, referred to as Lyα blobs (LABs; see Overzier 2016 for a review).

LABs are extended luminous Lyα sources, with $L_{\mathrm{Ly}\alpha} \sim 10^{43}$–$10^{44}$ erg s^{-1} and $\geqslant$50 kpc in size (Francis et al. 1996; Steidel et al. 2000; Dey et al. 2005; Yang et al. 2009, 2010; Ouchi et al. 2020). While what powers their emission remains

Original content from this work may be used under the terms of the Creative Commons Attribution 4.0 licence. Any further distribution of this work must maintain attribution to the author(s) and the title of the work, journal citation and DOI.

poorly constrained, possible mechanisms include galactic superwinds (Taniguchi & Shioya 2000), ionizing photons from star formation (Geach et al. 2016; Ao et al. 2017) and AGN activity (Dey et al. 2005; Geach et al. 2009; Yang et al. 2014a; Cai et al. 2017), resonant scattering of Lyα photons (Hayes et al. 2011; You et al. 2017; Kim et al. 2020; Chang et al. 2023), and gravitational cooling (Fardal et al. 2001; Rosdahl & Blaizot 2012; Daddi et al. 2021; Arrigoni Battaia et al. 2022). LABs often host multiple galaxies and are sometimes associated with overdense regions (Steidel et al. 2000; Matsuda et al. 2004, 2011; Prescott et al. 2008; Yang et al. 2010; Bădescu et al. 2017; Kikuta et al. 2019) or cosmic filaments (e.g., Erb et al. 2011; Umehata et al. 2019), providing a promising pathway to study protoclusters.

How LABs are distributed within the large-scale structure remains unclear. Some studies find tentative evidence that the morphologies of LABs are aligned with the large-scale structure (e.g., Erb et al. 2011; Kikuta et al. 2019) and that the brightest blobs tend to lie near the densest regions (e.g., Kikuta et al. 2019). Meanwhile Bădescu et al. (2017) observed that LABs appear to avoid the most overdense regions and to prefer the outskirts of massive structures. Other studies find that not all LABs reside in overdense environments (e.g., Hibon et al. 2020). Many of these results are based on a single protocluster and/or a small sample of LABs, making it difficult to account for the effect of cosmic variance properly and to address the question of how reliably LABs trace protocluster sites. To make significant progress, it is essential to study the relationship between LABs and their large-scale environment in a statistical manner.

One efficient way to achieve this goal is by conducting a narrow-band (NB) imaging survey aimed at finding both LABs and the more compact and commonplace LAEs. LAEs are generally young, low-mass star-forming galaxies (Gawiser et al. 2006a, 2007; Guaita et al. 2011) whose relatively low galaxy bias ($b \approx 2$) and low luminosity imply that they trace the bulk of the high-redshift galaxy population (Gawiser et al. 2007), making them ideal tracers of large-scale structure (e.g., Huang et al. 2022). Simultaneously, Lyα emission at $z \gtrsim 2$ is redshifted into the visible window, facilitating detection over large areas from the ground using wide-field imagers.

In this work, we utilize the early science data from the ongoing One-hundred-deg^2 DECam Imaging in Narrowbands (ODIN) survey, the widest field NB survey to date. The large sample of LAEs (5352) selected over a wide (9.5 deg^2) contiguous field allows us to peer into a well-defined slice of the cosmos in which groups, filaments, and voids are readily visible. Equipped with this information, we investigate where 129 LABs at $z = 3.1$ live in the context of the large-scale structure spanning hundreds of comoving megaparsecs. Through this work, we hope to demonstrate the power of wide-field NB imaging in illuminating cosmic structure formation in ways that cannot be easily replaced by the upcoming ELTs.

This paper is organized as follows. In Sections 2 and 3, we describe the imaging data and the selection of the LAE and LAB samples, respectively. In Section 4, we explore multiple methods to map large-scale structure using LAEs as tracers. We examine the relationship of LABs with the measured large-scale environment in Section 5 and summarize our findings in Section 6. Throughout this paper, we adopt a cosmology with $\Omega = 0.27$, $\Omega_\Lambda = 0.73$, $H_0 = 70$ km s^{-1} Mpc^{-1} (Komatsu et al. 2011). Distance scales are given in comoving units of h_{70}^{-1} cMpc, with the h_{70} suppressed unless noted otherwise. All magnitudes are given in the AB system (Oke & Gunn 1983).

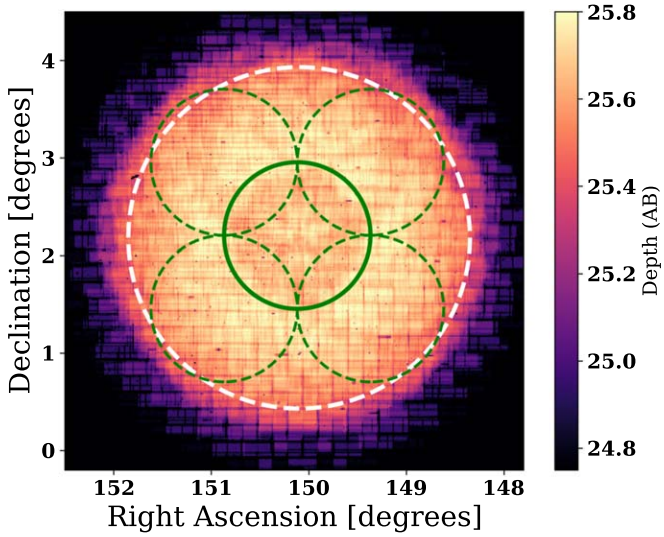

Figure 1. The 5σ depth of the ODIN E-COSMOS *N*501 data is indicated by the color bar on the right. The white dashed line indicates the anticipated coverage of the LSST Deep Drilling Field. Green circles mark the positions of the SSP Deep (dashed) and UltraDeep (solid) pointings.

2. Data and Catalogs

2.1. ODIN and SSP Imaging Data

As a survey program approved by the NSF's Optical-Infrared Laboratory, ODIN is currently undertaking the widest NB imaging survey to date using the Dark Energy Camera (DECam; Flaugher et al. 2015) on the Blanco Telescope at the Cerro Tololo Inter-American Observatory. Using three custom NB filters (*N*419, *N*501, and *N*673), ODIN is covering seven contiguous fields totaling 91 deg^2 in area, each sampled at three redshifts, $z = 2.4$, 3.1, and 4.5. The details of the survey design, data reduction, and calibration will be presented in a separate paper (K.-S. Lee et al. 2023, in preparation). In this work, we analyze a single ODIN field observed with our *N*501 filter. The filter characteristics ($\lambda_C/\Delta\lambda = 5015/73$ Å) are sensitive to redshifted Lyα emission at $z \sim 3.1$ ($3.09 < z < 3.15$). The data cover $\sim$12 deg^2 of the extended COSMOS field[16] with seeing 0.″9 at a near-uniform depth of 25.6 mag in the central 10 deg^2. The depth and coverage of the *N*501 data are shown in Figure 1.

We make use of the publicly available *grizy* broadband (BB) data from the HyperSuprimeCam Subaru Strategic Program (SSP; Aihara et al. 2018a, 2018b) from the second data release (Aihara et al. 2019). The sky area mapped by the SSP survey is smaller than the ODIN coverage, limiting the area in which LAEs can be selected to $\sim$9.5 deg^2. In Table 1, we list the 5σ limiting magnitudes of all bands. These are based on the 5σ fluctuations of the noise measured in randomly placed 2″ diameter apertures. The SSP coverage of the COSMOS field consists of one UltraDeep pointing and four Deep pointings (Aihara et al. 2018a), shown as green solid and dashed circles, respectively, in Figure 1. As a result, the variation of the BB

[16] Five of the ODIN fields are designed to match the LSST field of view of its Deep Drilling Fields and their pointing centers. For the COSMOS field, it is α = 10:00:24, δ = 02:10:55 (J2000).

Table 1
Details of COSMOS imaging data.

Band	Depth (Deep/UltraDeep)	Seeing
*N*501	25.6/25.6	0.″90
g	26.3/26.6	0.″81
r	26.0/26.2	0.″74
i	25.9/26.0	0.″62
z	25.8/26.0	0.″63
y	24.8/25.2	0.″71

Note. Median depth and seeing of the imaging data. The depth is measured as the 5σ fluctuations of the noise in 2″ diameter apertures.

imaging depths is significant. The effect of the depth variation on the detection of LAEs is discussed in Section 3.1.

The *N*501 data consist of 72 individual DECam exposures (each with an exposure time of 1200 s) taken in 2021 February; the total observing time is 24 hr for the field with a per pixel exposure time range of 20 minutes to 7.3 hr and an average of 2.9 hr or 3.1 hr (minimum of 1 or 2 overlapping exposures, respectively). Individual DECam frames are processed and coadded with the DECam Community Pipeline (Valdes & Gruendl 2014; Valdes 2021) into a single image.

Each of the 62 DECam CCDs is flat-fielded separately by dome flats, star flats, and dark sky illumination flats. Master dome flats are produced by stacking sequences of 11 exposures taken nightly. Star flats are produced periodically from 22 widely dithered exposures of a field with many bright stars using the algorithm of Bernstein et al. (2017). Dark sky illumination flats are created by coadding unregistered stacks of exposures.

The background is measured in blocks by the modes of nonsource pixels. The background is then made uniform by matching the means in each CCD and subtracting a low-order fit to the modes. While this step is critical to producing a uniform dithered stack, it leads to oversubtraction of the faint halos around bright stars. However, we remove any science source close to bright stars in the analysis by applying star masks (Section 2.2). Thus, the effect of uneven background levels near bright stars on the small, distant extragalactic objects is negligible.

An astrometric solution is derived for each CCD by matching stars to Gaia-EDR3 (Gaia Collaboration et al. 2021). The higher-order distortions are predetermined and fixed, and the low-order terms are updated using the astrometric solver SCAMP (Bertin 2006) with continuity constraints between CCDs. The solution rms is typically tens of milliarcseconds. The solution is used to reproject the exposures to a standard tangent plane sampling with constant pixel sizes using sinc interpolation. A fixed tangent point for all the exposures in the field is used. The exposures are matched to the Pan-STARRS-1 photometric catalog (Schlafly et al. 2012) for a flux zero-point to provide the scaling and, along with seeing and sky brightness estimates, weighting of the coadded image. The dithered exposures are stacked by averaging registered pixels with statistical rejection (constrained sigma clipping) of outliers to minimize cosmic rays accumulated from the long exposures.

Following the format of the SSP data release, the final ODIN stack is split into multiple "tracts," each $1.^{\circ}7 \times 1.^{\circ}7$ in size with an overlap of 1′. The SSP tracts are reprojected using the DECam Community Pipeline to have the same tangent points and pixel scales (0.″26) as the ODIN data.

2.2. Source Detection.

Source detection is conducted using the SOURCE EXTRACTOR software (Bertin & Arnouts 1996) run in dual-image mode using the *N*501 band data as the detection image while performing photometry in all bands. For point-spread function (PSF)-matched photometry, rather than degrading the images with smoothing kernels, we measure the flux in successive, closely spaced apertures. The appropriate aperture correction for a given band is computed by requiring that the fraction of the flux enclosed remains constant. Regardless, for the aperture size we choose for LAE selection (2″ diameter) the correction is minimal for all filters. Assuming a Moffat profile with $\beta = 2.5$, the aperture correction factor for a point source varies from 1.07 to 1.09 when seeing changes from 0.″6 to 1.″0.

A great majority of LAEs are expected to be point sources at $z = 3$ (Malhotra et al. 2012; Paulino-Afonso et al. 2018). Prior to source detection, all images are convolved with a Gaussian filter (`FILTERING = Y`) with an FWHM matched to the seeing value of the *N*501 data, optimizing for the detection of point sources (Gawiser et al. 2006b). The detection threshold in the filtered image is set to 0.95σ and the minimum area is set to 1 pixel (`DETECT_THRESH = 0.95` and `DETECT_MINAREA = 1`). The choice of `DETECT_THRESH` is motivated by running SOURCE EXTRACTOR on sky-subtracted and inverted (or "negative") versions of our science images. In these negative images, any detected sources are due to noise fluctuations, as all the true sources will have pixel values well below zero. If the noise is Gaussian, the fluctuations of the sky value both above and below the mean should be the same; thus, the number of sources detected in the negative images should represent the extent of the contamination of the source catalog by noise peaks. To maximize the detection of faint sources, we choose the minimum value of `DETECT_THRESH` that yields a contamination fraction of less than 1%. We remove objects with a signal-to-noise ratio (S/N) less than 5 in a 2″ diameter aperture ($N501 \gtrsim 25.6$) and sources with internal flags `FLAG` $\geqslant$ 4—suggesting that they contain saturated pixels or significant image artifacts—from our catalog. We also use the star masks released as part of the SSP DR2 (Coupon et al. 2018) and remove all sources near bright stars. Accounting for the sky area excluded by these masks, the effective area covered by our catalog is $\sim$7.5 deg^2, and the total number of *N*501-detected objects after making these cuts is 689,962.

2.3. Simulations

While a detailed comparison of our results with the expectations from state-of-the-art hydrodynamic simulations is beyond the scope of this work, we make use of the IllustrisTNG simulations here to build cosmologically sound expectations for how cosmic structures may manifest themselves in observations such as ODIN. To this end, we use the IllustrisTNG300-1 (hereafter TNG300) simulation, the largest box with the highest resolution available from the IllustrisTNG suite (Pillepich et al. 2018a, 2018b; Nelson et al. 2019). TNG300 represents a periodic box of 302.6 cMpc on a side and is run from $z = 127$. The cosmological parameters for the TNG simulation are different from ours.[17]

[17] The IllustrisTNG simulations adopt the Planck cosmology (Planck Collaboration et al. 2016): $\Omega_\Lambda = 0.6911$, $\Omega_b = 0.0486$, $\Omega_m = 0.3089$, and $H_0 = 100\,h$ km s^{-1} Mpc^{-1} with $h = 0.6774$

In addition to the publicly available TNG data, we also make use of the UV magnitudes computed by Vogelsberger et al. (2020). An Lyα luminosity is assigned to each halo following the prescription given in Dijkstra & Wyithe (2012) and Weinberger et al. (2019). Both the UV and Lyα luminosity functions computed within the full TNG300 volume are in good agreement with the measurements in the literature. A full description of the procedures and the predictions for protocluster galaxy populations will be presented in M. C. Artale et al. (2023, in preparation).

3. Sample Selection

3.1. LAE Selection

The details of the ODIN LAE selection methods will be presented in a forthcoming paper (N. Firestone et al. 2023, in preparation) and we only briefly summarize them here. We select LAEs as sources with an NB excess, based on the NB-continuum color. Gronwall et al. (2007) and Gawiser et al. (2007) found that $z \sim 3$ LAE samples selected via an NB excess corresponding to rest-frame equivalent width $W_0 > 20$ Å suffer greater contamination from continuum-only objects than from [O II] emitters. In order to obtain a robust estimate of the 501 nm continuum level of all objects in the catalog, we create a weighted average of the g- and r-band flux density in a 2″ diameter aperture, using weights determined from the central wavelengths of g, r, and $N501$ to estimate the flux density at 501 nm:

$$f_{gr} \equiv 0.83 f_g + 0.17 f_r. \quad (1)$$

We convert f_{gr} to an AB magnitude gr and select all objects with color excess $gr - N501 > 0.82$, which corresponds to $W_0 > 20$ Å following the equation:

$$(gr - N501) > 2.5 \log\left(1 + \frac{[\lambda_{\rm eff}/\lambda_{{\rm Ly}\alpha,0}]\, W_0}{\Delta\lambda_{N501}}\right), \quad (2)$$

where $\Delta\lambda_{N501}$ is the FWHM of the $N501$ filter transmission (72.5 Å), $\lambda_{{\rm Ly}\alpha,0}$ is the rest-frame wavelength of Lyα (1215.67 Å), and $\lambda_{\rm eff}$ is the observed-frame Lyα wavelength, i.e., the central wavelength of $N501$ (5015 Å). Additionally, we remove all objects whose NB color excess is consistent with zero at the 3σ level to minimize contamination from continuum-only objects scattered into the color cut by requiring:

$$gr - N501 > 3\sigma_{gr-N501}. \quad (3)$$

The photometric scatter in the $gr - N501$ color, $\sigma_{gr-N501}$, is calculated by propagating the uncertainties of the flux densities in each band. The median color scatter is well fit by a second-order polynomial of the form, $\sigma_{gr-N501} = 5.2259 - 0.4934m + 0.01165m^2$, where m is the $N501$ magnitude. Our selection results in 5352 LAE candidates in our sample. In Figure 2, we plot the $gr - N501$ color versus the $N501$ mag for the full catalog along with the selected LAE candidates. The blue dashed line shows the functional form of the median $3\sigma_{gr-N501}$ line given above. Our chosen $gr - N501$ cut places our LAE candidates safely above the locus of continuum-only objects.

While we leave a detailed assessment of our LAE candidates for future work, the number of LAE candidates we find is in reasonable agreement with the expectations from previous studies. Gronwall et al. (2007) found 162 $z = 3.1$ LAEs in 0.28 deg^2 with fluxes above 1.5×10^{-17} erg cm^{-2} s^{-1} with a 50 Å filter; Gawiser et al. (2007) reported a 20% uncertainty in the resulting LAE number density once cosmic variance due to large-scale structure is included. Ciardullo et al. (2012) found 130 $z = 3.1$ LAEs in 0.28 deg^2 with fluxes above 2.4×10^{-17} erg cm^{-2} s^{-1} with a 57 Å filter. Accounting for the width of our filter and conservatively assuming Poissonian errors, we would expect $\sim 6549 \pm 515$ LAEs based on the result of Gronwall et al. (2007) and 4887 ± 429 LAEs based on the result of Ciardullo et al. (2012) in our 7.5 deg^2 survey area. Given the differences in completeness and depth across various surveys, it is difficult to quantify the contamination fraction for our sample concretely based on these past works, but the good agreement of the observed LAE number density with the expectations suggests that the contamination fraction is low. A spectroscopic program to confirm a portion of our LAE candidates is ongoing, and the results of this program together with a proper estimation of the contamination fraction will be presented in a future work. We also note that since the contamination fraction should be more or less constant across the entire field, the presence of contaminants will not have a significant effect on the estimation of the LAE surface density, which is the main purpose of the LAE sample in the present work.

The depth variations of the SSP BB data across our survey field (see Table 1) should not significantly affect the LAE number density. While a greater BB depth would in principle reduce the uncertainty of the estimated gr magnitude, the uncertainty on the $gr - N501$ color excess is dominated by the photometric scatter in the $N501$ band, which has a uniform coverage. This can be seen in Figure 2, where the median $3\sigma_{gr-N501}$ value is very small for sources with bright $N501$ magnitudes and increases rapidly with increasing $N501$ magnitude. Indeed, we find that the LAE number density in the UltraDeep region (790 deg^{-2}) is consistent with that in the Deep region (756 deg^{-2}) within the Poisson uncertainties.

3.2. LAB Selection

The details of the final selection of ODIN LABs will be presented in another paper (B. Moon et al. 2023, in preparation). Here, we provide a brief description. Our selection method is similar to those used in previous blind LAB searches (e.g., Matsuda et al. 2004; Yang et al. 2010). To look for extended Lyα emission, we select LABs in two steps: (1) identifying objects with an NB-to-BB color excess (i.e., as LAEs) and (2) detecting extended Lyα emission around them from a continuum-subtracted Lyα image.

To detect the bright core of LABs, we first create another LAE catalog using detection settings and color criteria that are slightly different than those given in Sections 2.2 and 3.1. We choose a higher `DETECT_THRESH` of 1.2σ and a larger `DETECT_MINAREA` = 4 to exclude faint sources that are associated with spurious low surface brightness features. Then, we apply the following criteria: (1) $N501 < 25.62$ and (2) $gr - N501 > 0.8$, where all fluxes and magnitudes are measured in a 2″ diameter aperture.

To detect extended Lyα emission, we create an Lyα image by subtracting the continuum flux from the $N501$ image, with the continuum flux estimated from the g and r bands as described in Section 3.1. The BB images are smoothed with a Gaussian kernel to match their PSF sizes with the NB image

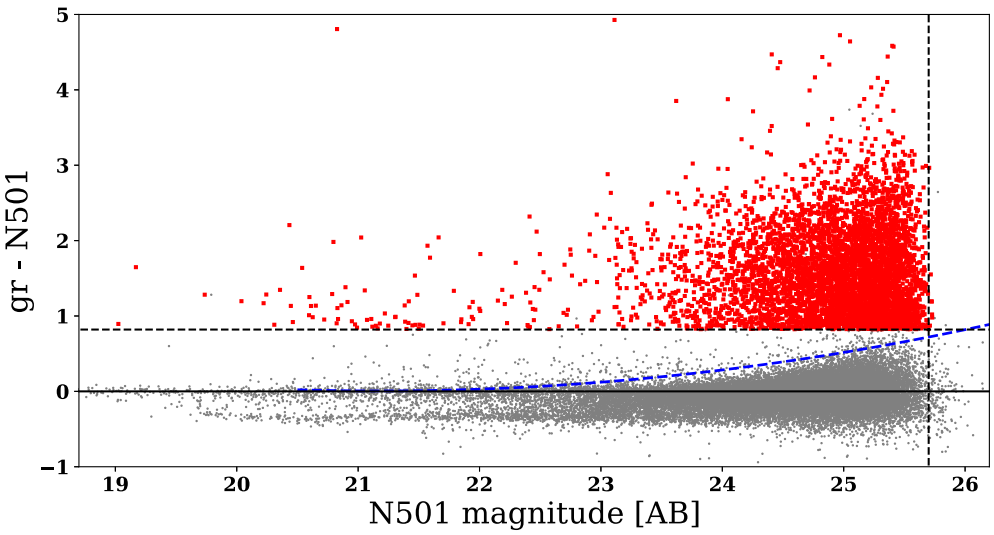

Figure 2. NB-to-BB color excess ($gr - N501$) vs. $N501$ magnitude. Red points represent LAE candidates. Gray dots show 1 in every 20 $N501$-detected sources that are not LAEs. Black dashed lines mark the color cut corresponding to $W_0 = 20$ Å (horizontal) and 5σ limiting magnitude of the $N501$ data (vertical), respectively. The blue dashed line shows the median $3\sigma_{gr-N501}$ line as a function of $N501$ magnitude.

before the continuum subtraction. We generate a mask for areas with negative sky counts and halos around saturated stars in the gr bands, which can mimic diffuse emission. The mask is used as `MAP_WEIGHT` to prevent the detection of such features. After filtering the image with a 7 pixel 2D Gaussian filter with an FWHM of 3 pixels, we detect all sources with contiguous isophotal size greater than 42 pixels ($\sim$3 arcsec^2) all of which rise above the surface brightness threshold of 3.3×10^{-18} erg s^{-1} cm^{-2} arcsec^{-2}. The value corresponds to 1.5σ where σ is the pixel-wise sky rms measured in the Lyα image. From the sources with isophotal size over 3 arcsec^2, we select those with an isophotal area greater than 20 arcsec^2. We further require that at least one LAE coincide with the extended emission for the source to be considered an LAB candidate.

In Figure 3, we show as red circles the distribution of isophotal sizes ($A_{\rm iso}$) and $L_{{\rm Ly}\alpha}$ of all recovered sources. Gray dots represent similar measurements made for simulated point sources. To guard against bright point sources being selected as LABs, we require that LAB candidates lie above the 3σ line of the known $A_{\rm iso} - L_{{\rm Ly}\alpha}$ relation for point sources and that $A_{\rm iso} \geqslant 20$ arcsec^2. This minimum area threshold is of the same order as those adopted by previous NB surveys for LABs (e.g., Matsuda et al. 2004; Yang et al. 2009, 2010). The precise LAB selection criteria were determined after extensive tests, varying the minimum area and the surface brightness threshold while visually inspecting the resulting LAB candidates. These tests suggest that most of the additional LAB candidates selected by relaxing $A_{\rm iso}$ to a lower value (such as 16 arcsec^2, similar to Matsuda et al. 2004) are spurious. A quantitative comparison of various LAB selection criteria will be provided in a forthcoming paper (B. Moon et al. 2023, in preparation). These criteria are indicated by blue lines in Figure 3. A total of 129 LAB candidates are identified in our final sample; these are shown in Figure 3 as large red circles highlighted in blue.

Given the differences in sensitivity of various surveys, differences in selection criteria, and strong field-to-field variations (Yang et al. 2010), it is difficult to compare the number density of our LAB candidates directly with those found in existing surveys. As the ODIN survey progresses further, we will robustly quantify these variations based on the LAB statistics from seven widely separated fields at a uniform depth.

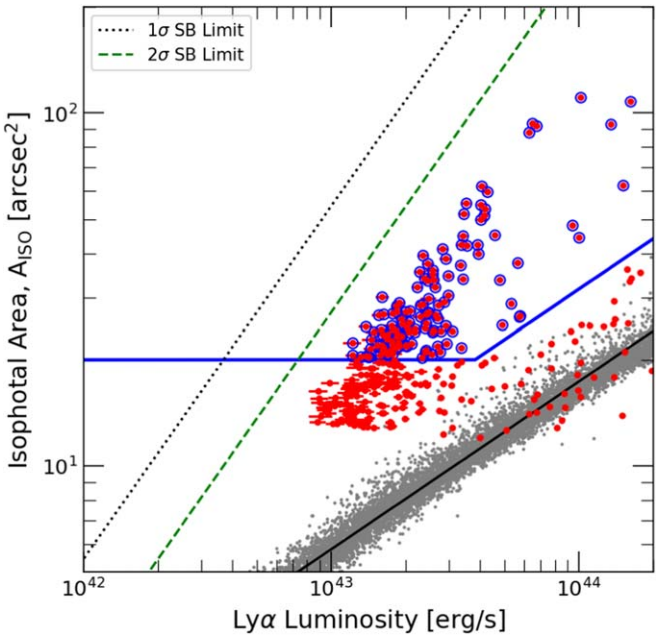

Figure 3. Positions of our LAB candidates are shown as large red circles highlighted in blue on the $A_{\rm iso}$–$L_{{\rm Ly}\alpha}$ space. Small red circles mark all the sources with $A_{\rm iso} > 3$ arcsec^2 while gray dots and the thick solid line indicate the locations of simulated point sources and the best-fit scaling law, respectively. Blue solid lines outline the final LAB selection criteria: (1) $A_{\rm iso} > 20$ arcsec^2 and (2) sources lie $>3\sigma$ above the relation of point sources. The diagonal dotted and dashed lines correspond to the 1σ and 2σ surface brightness limits, respectively.

Figure 4 shows one of our LAB candidates in the $grN501$ bands as well as the Lyα image. The source has $L_{{\rm Ly}\alpha} = 6.5 \times 10^{43}$ erg s^{-1} and $A_{\rm iso}$=96 arcsec^2. Several galaxies lie within or near the LAE region, which extends to $\approx$100 kpc. These characteristics are similar to LABs discovered in the past (e.g., Steidel et al. 2000; Matsuda et al. 2004; Yang et al. 2011, 2014b; Prescott et al. 2012).

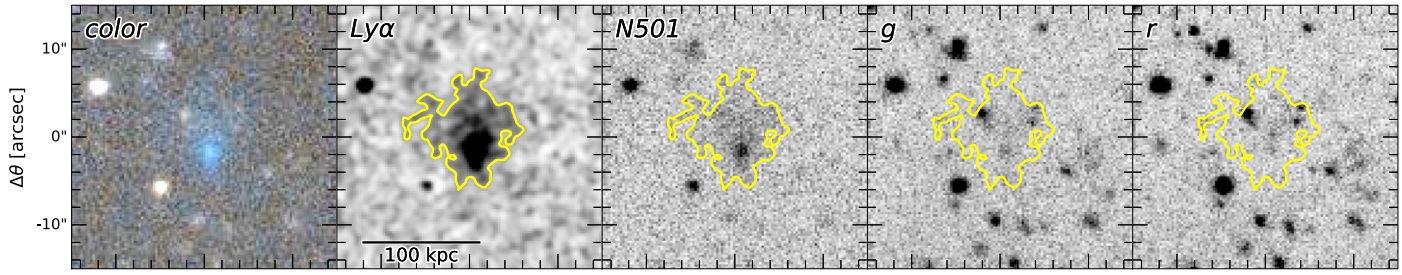

Figure 4. An ODIN LAB at $z = 3.1$ with spectroscopic confirmation. The postage stamp images are 30″ on a side. The color image (left-most) is created with the DECaLS *rg* and *N*501 data respectively used to make the RGB image. The BB and NB images are from the SSP and ODIN *N*501 data. In the four right panels, yellow contours outline our SB threshold, 3.3×10^{-18} erg s^{-1} cm^{-2} arcsec^{-2}. Multiple galaxies are found within or near the LAE region, which extends nearly ≈100 kpc.

In spring 2022, several LAB candidates were targeted by a Gemini/GMOS program and subsequently confirmed, which includes the LAB shown in Figure 4. Follow up of more LAB targets is scheduled in 2023. While the full results of the spectroscopic programs will be presented elsewhere, Figure 5 shows the 1D Lyα spectrum for the LAB. The black line indicates the *N*501 transmission normalized arbitrarily. The profile shows a very wide width (∼1400 km s^{-1}, FWHM) and a double-peaked line profile with a weaker blue peak, characteristic of Lyα emission. The absence of any other emission lines (e.g., Hα, Hβ, [O III]) makes it very unlikely that the source is an [O II] or [O III] emitter at lower redshift. Furthermore, it is unlikely for lines other than Lyα to display the observed extended emission, since they do not undergo resonant scattering. In addition to the spectroscopically confirmed LABs, our selection recovers RO-0959, a known LAB at $z = 3.096$ published by Daddi et al. (2021), even though its line emission falls on the edge of the *N*501 transmission. Confirmation of these LABs lends support to the robustness of our LAB selection.

4. Tracing the Large-scale Structure with LAEs

Galaxies are biased tracers of the underlying matter distribution. Thus, once the galaxy bias of a given population is known, their positions can be used to map large-scale structure. Generally, existing studies have found that more-massive or more-luminous galaxies tend to have higher galaxy biases than their less-luminous cousins as they occur preferentially in high-density peaks (Kaiser 1984; Davis et al. 1985; Norberg et al. 2002). Existing studies also suggest that LAEs have the lowest bias value of all probed galaxy populations at high redshift (∼2; Gawiser et al. 2007; Guaita et al. 2010; Hong et al. 2019; Khostovan et al. 2019). Their high abundance and low bias make them excellent tracers of the underlying matter distribution (see, e.g., Huang et al. 2022). Here, we study the large-scale structure at $z \sim 3.1$ traced by the LAEs in our sample. One caveat, however, is that LAEs, particularly those in the most overdense regions, could be hidden by dense clouds of H I gas (e.g., Shimakawa et al. 2017; Momose et al. 2021). This could cause us to underestimate the surface density toward the cores of protoclusters.

In Figure 6, we show the distribution of the LAE surface density across the field by placing a 5 cMpc (2.′6) radius circle on 20,000 randomly chosen positions and measuring the number of LAEs enclosed therein. If LAEs show no clustering, they are expected to obey a Poisson distribution as shown by the solid gray line. The fact that the distribution shows a significant excess at high surface densities strongly suggests that they are in fact clustered.

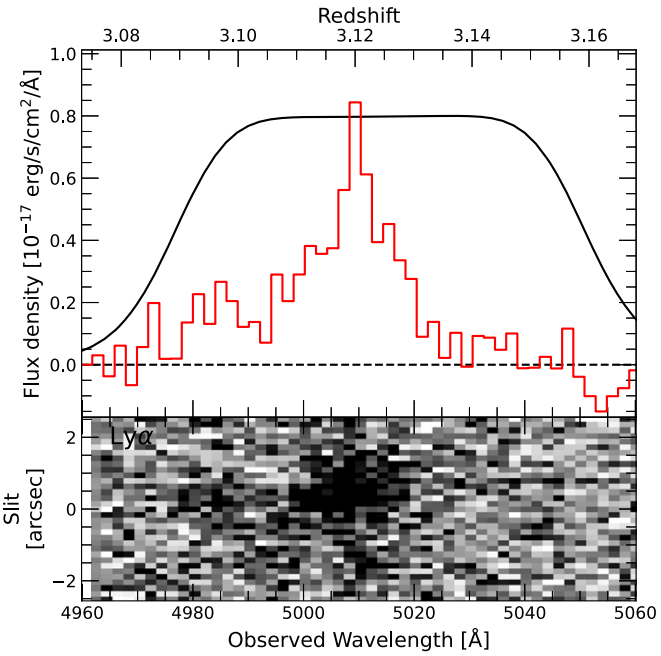

Figure 5. 1D and 2D spectra from the LAB shown in Figure 4. Gemini/GMOS reveals spatially extended and diffuse Lyα emission in the 2D spectrum. The 1D spectrum, extracted from the 2D spectrum, shows a double-peaked Lyα profile. The black line represents the transmission curve of *N*501 in arbitrary units.

We repeat the measurements using the LAEs modeled in the TNG300 simulations. The line-of-sight "thickness" of our data determined by the *N*501 filter transmission is matched by carrying out the measurements on a randomly chosen $300 \times 300 \times 60$ cMpc cosmic volume sliced along the *x*-, *y*-, or *z*-direction of the simulation. The results are shown in orange. While the simulated LAE counts are slightly over-predicted at the high-density end, the overall distributions of the real and simulated LAEs are qualitatively similar with a well-matched peak occurring at ≈0.2 arcmin^{-2}. The significant excess of the regions of high LAE densities seen in both data and simulations suggests the presence of large cosmic structures.

In this section, we explore different ways to use LAEs as tracers of cosmic structures, thereby detecting the groups, protoclusters, and filaments of the cosmic web.

4.1. Gaussian Kernel Smoothed Density Map

The simplest and the most commonly used method of creating a surface density map is by smoothing the LAE distribution with a fixed kernel such as a Gaussian, to produce a

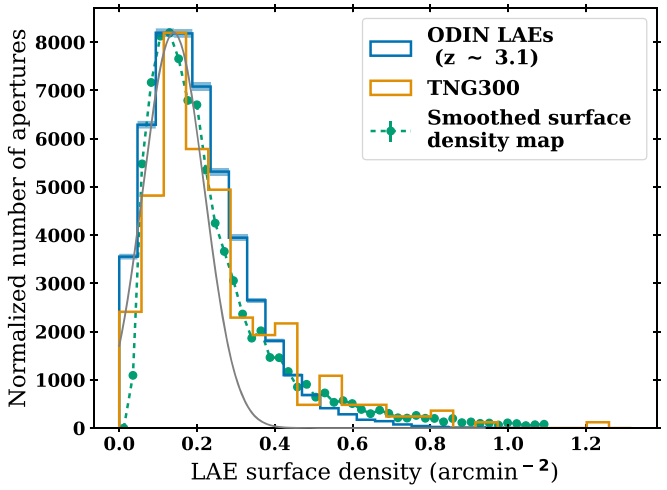

Figure 6. The distribution of LAE surface densities measured within randomly distributed 5 cMpc radius circular apertures is shown in blue. Similar measurements made on the TNG300 simulations (orange) with a line-of-sight thickness that matches the NB width are in reasonable agreement with our data. The green histogram shows the LAE density map constructed by smoothing the LAE positions with a Gaussian kernel (Section 4.1). All three exhibit a clear excess at the high-density end over a Gaussian approximation of the Poissonian function expected for a purely random distribution. In both data and simulations, the highest LAE overdensity regions trace the largest cosmic structures.

Gaussian smoothed (GS) map) (e.g., Yang et al. 2010; Lee et al. 2014; Saito et al. 2015; Bădescu et al. 2017; Shi et al. 2019; Zheng et al. 2021; Huang et al. 2022). In addition to being straightforward to implement, this method produces a visualization that is easy to understand.

We begin by creating a map of the LAE number density measured in bins of size 0.01° to a side (1.15 cMpc at $z = 3.1$). The empty regions left by bright stars and image defects are filled in by populating uniformly distributed random points that match the mean density of the field. A uniform random distribution is a reasonable approximation of the LAE distribution since, as discussed in Section 3.1, the LAE surface density is determined predominantly by the NB depth, which is highly uniform in our data (see Figure 1). The map is then convolved with a Gaussian kernel whose size is determined using kernel density estimation (KDE) following the method given in Bădescu et al. (2017).

In KDE, an estimator $\hat{f}(x)$ is created for the underlying distribution $f(x)$ from which a set of data points arises by smoothing the data with a predetermined kernel. The best kernel size, referred to as the bandwidth in KDE, is determined via the leave-one-out cross-validation scheme as follows. The estimator $\hat{f}_{-i}(x;\,\sigma)$ is found using a Gaussian kernel with width σ and leaving out the ith data point x_i. The likelihood of the estimator yielding the ith data point is $\hat{f}_{-i}(x_i;\,\sigma)$. The σ value that optimizes the likelihood of finding all data points is the one that maximizes $\prod_i \hat{f}_{-i}(x_i)$. For our LAE sample, the optimal Gaussian kernel has FWHM $= 5\farcs2$ (10 cMpc at $z = 3.1$). This kernel size is comparable to the expected size of a protocluster (Chiang et al. 2013). The distribution of the LAE surface density using this method is shown in Figure 6 (green), consistent with other measurements therein.

The LAE (surface) overdensity is computed as:

$$\delta_{\rm LAE} = \frac{\Sigma_{\rm LAE}}{\overline{\Sigma}_{\rm LAE}} - 1, \qquad (4)$$

where $\overline{\Sigma}_{\rm LAE}$ and $\Sigma_{\rm LAE}$ are the mean and local LAE density, respectively. The mean density and its standard deviation are determined by fitting the $\Sigma_{\rm LAE}$ histogram with a Gaussian function of the form $\exp[-(N-\mu)^2/2\sigma^2]$. The fitting is done after sigma clipping the high tail with a threshold of 1.5σ, retaining only the low end of the distribution which is representative of the field for the fitting. A Gaussian function is expected to be a good fit to the low end of the surface density distribution (e.g., Chiang et al. 2014; Araya-Araya et al. 2021); this is also seen in Figure 6. We find $\mu = 0.14$ arcmin^{-2} and $\sigma = 0.08$ arcmin^{-2}, respectively.

In the top panel of Figure 7, we show the relative LAE density, $(1+\delta_{\rm LAE})$. The contours indicate overdensities at the 2σ (black), 3σ (green), 4σ (blue), and 5σ (white) levels. In the forthcoming discussion, we refer to LAE overdensities of 2–3σ as "moderate" densities and LAE overdensities of $>3\sigma$ as "high" densities. Multiple large complexes of overdensities are visible within which several hundreds of LAEs reside. Three of the largest complexes, labeled as A, B, and C in the figure, are shown in the bottom panels of Figure 7 where individual LAE positions are indicated. The morphology of these LAE overdensities is strikingly irregular, which we summarize below.

1. *Complex A*: the largest structure in our map—has at least four individual groups. In addition, an elongated moderate-density structure (labeled A1) extends northeast from the largest group. The configuration is reminiscent of a filamentary arm connected to a massive halo.
2. *Complex B*: similar to A, multiple regions of overdensities are connected by "bridges" (one of them labeled B1) of more moderate overdensity. B1 is not captured well in this smoothed density map. This topic will be revisited in Section 4.2.
3. *Complex C*: an extended structure (C1) is connected to a more overdense one (C2) via a filament. Once again, the filament is not evident from the contour lines but can be seen from the alignment of LAEs stretching out from C2 southward.

The features seen in these complexes—such as elongated structures, clumpy morphology, and filaments connecting large structures—are similar to those seen in cosmological dark matter simulations (e.g., Boylan-Kolchin et al. 2009; Kuchner et al. 2022), and are in qualitative agreement with expectations from the hierarchical theory of structure formation.

While the Gaussian kernel smoothing method does an excellent job of pinpointing significant overdensities, it does not fare well in detecting intermediate-density features such as filaments. This shortcoming is tied to the choice of the smoothing scale (10 cMpc), which is applied in all directions. Any structure whose size is comparable to or larger than this value would stand out clearly in the smoothed map whereas those smaller or narrower than this scale would not. To circumvent this challenge, we take a scale-free approach in Section 4.2.

4.2. Voronoi Tessellation

Tessellation-based methods perform well at finding small-scale and/or anisotropic structures (Darvish et al. 2015) and have been employed in several recent studies (e.g., Dey et al. 2016; Cucciati et al. 2018; Lemaux et al. 2018; Hung et al. 2020;

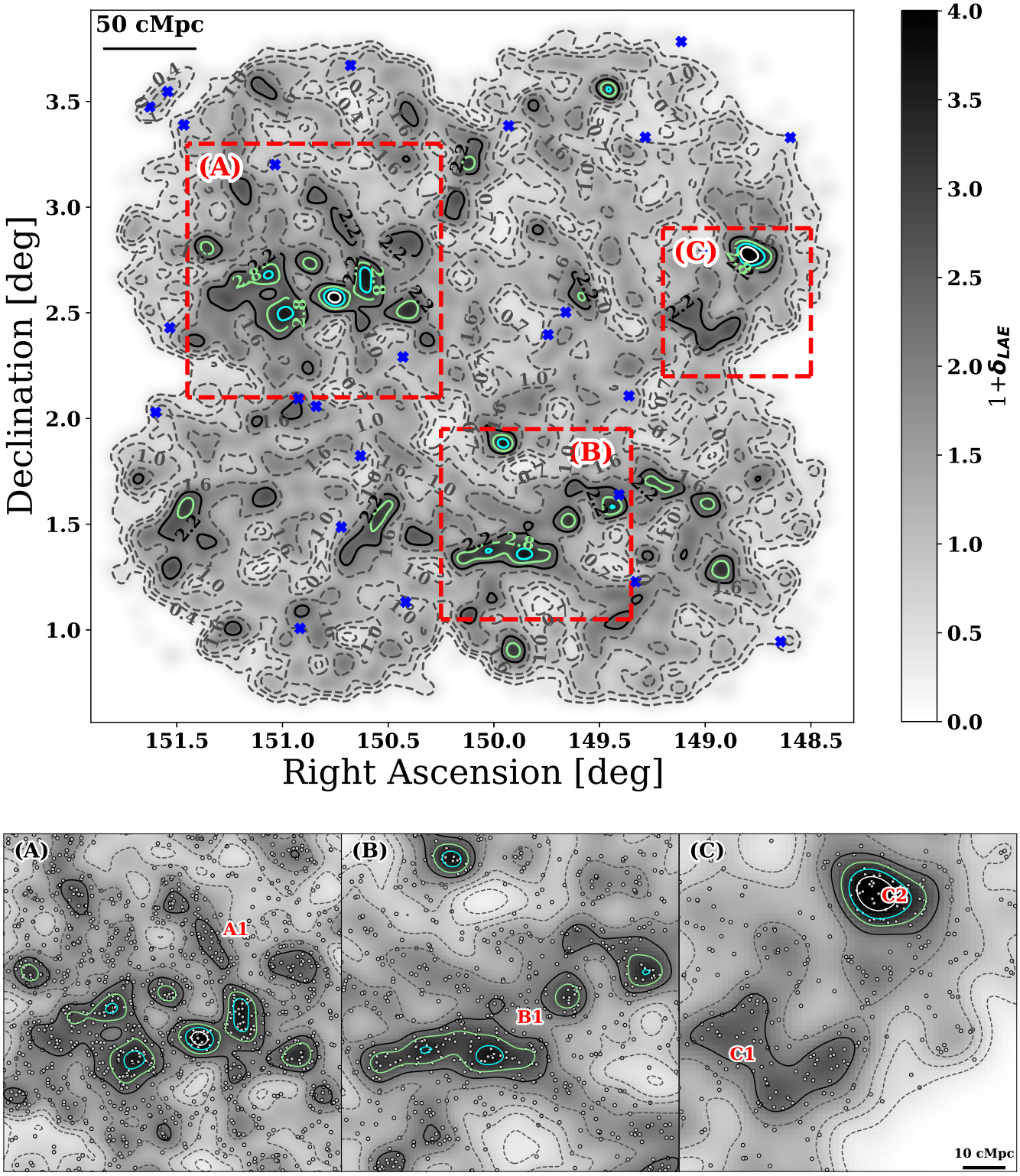

Figure 7. Top: LAE overdensity map constructed from the Gaussian kernel smoothing method (Section 4.1) is shown in both greyscale and contour lines. Black, green, blue, and white contours indicate overdensities with $\delta_{\rm LAE}$ 2, 3, 4, and 5σ above the field value, respectively. The position of the holes left by bright stars, which are filled in with uniformly distributed random points, are indicated by blue crosses. Bottom: zoomed-in views of the three regions outlined by dashed rectangles. Individual LAEs are indicated as gray dots. Some features of interest are labeled.

Malavasi et al. 2021). Here, we apply the Voronoi tessellation (VT) method to the LAE positions.

VT takes the locations of a set of points and partitions the space occupied by them into cells. Each cell is constructed to contain one generating point (in this case, a galaxy) and is comprised of the points that are closer to the enclosed generating point than any other. The size of a Voronoi cell is a measure of the density of the surrounding region, i.e., cells that fall in an overdense (underdense) region will be smaller (larger) in area than that of an average LAE.

We estimate the LAE surface density as follows. First, we calculate the area of the Voronoi cells, A_V, corresponding to each LAE. Any cell larger than 0.01 deg^2 ($\sim$130 cMpc^2 at $z = 3.1$) is excluded from further analysis as such cells are unphysically large. Visual inspection confirms that these cells are unbounded and are located at the edges of the image. Such cells comprise $\approx$2% of the total number. The surface density of an LAE is the inverse of the area of the Voronoi cell in which it is located.

Following the prescription given in the literature (e.g., Cucciati et al. 2018; Lemaux et al. 2018; Hung et al. 2020), we construct a pixellated density map based on VT by populating the field with a uniform grid of points; the spacing of the grid is 3.″6 (0.12 cMpc), much smaller than the Voronoi polygons. All points within a given polygon are assigned the same density ($=1/A_V$).

Similar to the GS map, the mean density is determined by fitting the density histogram with a Gaussian function. We find that the best-fit parameters are $(\mu, \sigma) = (0.10, 0.06)$ arcmin^{-2}, in reasonable agreement with those determined in Section 4.1. The overdensity map is generated using Equation (4).

The resultant map is shown in the top panel of Figure 8 and reveals the same structures discussed in Section 4.1. As expected, the tessellation method fares better in detecting smaller and more irregular structures. In this context, we reexamine complexes A, B, and C. To facilitate comparison, we display the GS map 2σ and 3σ contours in pink.

1. *Complex A*: the filamentary arm-like structure labeled as A1 is more clearly detected in the VT map compared to the GS map (Figure 7, bottom left). It is detected at the same significance as the galaxy group to which it is connected.
2. *Complex B*: similarly to A, the "bridge" labeled B1 connecting the largest elongated structure to a smaller one in the northwest is clearly detected at a high significance. This feature is not fully captured in the GS map. Several smaller overdensities in the region labeled B2 are newly detected in the VT map.
3. *Complex C*: the irregular overdensity in the southeast (C1) is clearly delineated with a higher significance than previously. The region labeled C3 connecting the two largest overdensities (C1 and C2) is newly detected in the VT map.

All in all, many of the most significant structures have clumpy/irregular morphologies consisting of multiple closely clustered overdensities, which are often joined together by bridges of moderate density. These features are in qualitative agreement with the expectations from the hierarchical theory of structure formation and affirm the notion that LAEs do trace the underlying large-scale structure of matter distribution, including the cosmic web.

4.3. Detection of Cosmic Structures

In this section, we describe how we identify cosmic structures at $z = 3.1$ traced by LAEs, by using the density maps discussed in Sections 4.1 and 4.2. We refer to these LAE-overdense structures as protoclusters, used in a broad sense. First, from the GS map, we define overdense structures as regions enclosed by the 3σ contours corresponding to $(1 + \delta_{\rm LAE}) = 2.84$ with a minimum area of 78.5 cMpc^2 ($\sim$22 arcmin^2). The motivation for the latter requirement is to ensure that the projected size of a detected structure is at least as large as that of the adopted kernel ($\pi \cdot 5^2 = 78.5$). While the condition would be easily satisfied by any protocluster,[18] it may exclude smaller groups unless they are close to the main halo.

For each structure, we assign the geometric center of the contour as its center. In most cases, the center location does not change significantly even if we define it as the peak density region instead. Out of the 12 structures we detect, three have coordinates offset by more than 2.′6 ($\sim$5 cMpc). These are located at $(\alpha, \delta) = (149.9°, 1.4°)$, (150.7°, 2.6°), and (151.1°, 2.7°). These protoclusters are irregular/elongated in their morphology; for example, the protocluster at (150.7°, 2.6°) is clearly a blend of two systems (as seen in Figure 9) and should perhaps not be treated as one. The optimization of protocluster/group selection will be presented in future work. At present, we note that even using the density peak as the center of the structures instead of the geometric center, our results remain qualitatively unchanged.

We also utilize the VT map to detect structures adopting a procedure similar to those in the literature (e.g., Lemaux et al. 2018; Hung et al. 2020; Sarron & Conselice 2021). We use SEP (Barbary 2016), a Python implementation of the SOURCE EXTRACTOR software. Prior to detection, we internally smooth the VT map with a Gaussian kernel with FWHM = 5 cMpc. Doing so helps to minimize the number of false detections and obtain relatively smooth boundaries for a given structure. As expected, the number of detections depends sensitively on the threshold and the minimum area. We adopt `DETECT_THRESH` = 4σ, corresponding to an absolute LAE overdensity value of 2.4, and `DETECT_MINAREA` = 7.7 arcmin^2 (25 cMpc^2). Once again, the latter is comparable to the smoothing scale, i.e., detected structures are always larger. Since the smoothing kernel is smaller than the required minimum area, the shapes of the detected overdensities are not significantly affected by the smoothing. This can be seen in the right panel of Figure 9 where the shapes of the regions selected as overdensities are reasonably well preserved. The former is chosen based on the result of Chiang et al. (2013), who find that protoclusters with descendant mass $\gtrsim 3 \times 10^{14}\ M_\odot$ should display NB-selected LAE overdensities of $\sim$1.5–2.5. We leave a detailed discussion of the protocluster selection parameters to a forthcoming paper (V. Ramakrishnan et al. 2023, in preparation)

In Figure 9, we illustrate the extent of the detected structures and their centers in complex A identified from the GS and the VT maps. While the five largest overdensities are detected by both with similar sizes, the VT method fares better at picking up smaller and/or more irregular overdensities. For example, the filament extending northeast (labeled A1 in Figures 7 and 8) is only detected in the VT map. It also performs better at separating nearby structures. The pair of overdensities around (150.6°, 2.6°) is identified in the GS map as one structure. Overall, we find that the VT method is preferable for structure detection to fixed kernel smoothing. However, we make use of both sets of structures in the subsequent analysis to demonstrate the robustness of our results against the specifics of structure detection.

[18] A protocluster at $z = 3$ that will evolve into a galaxy cluster with masses $M_{z=0} \geqslant 10^{14}\ h_{100}^{-1} M_\odot$ has a half mass radius of 5–10 cMpc (Chiang et al. 2013)

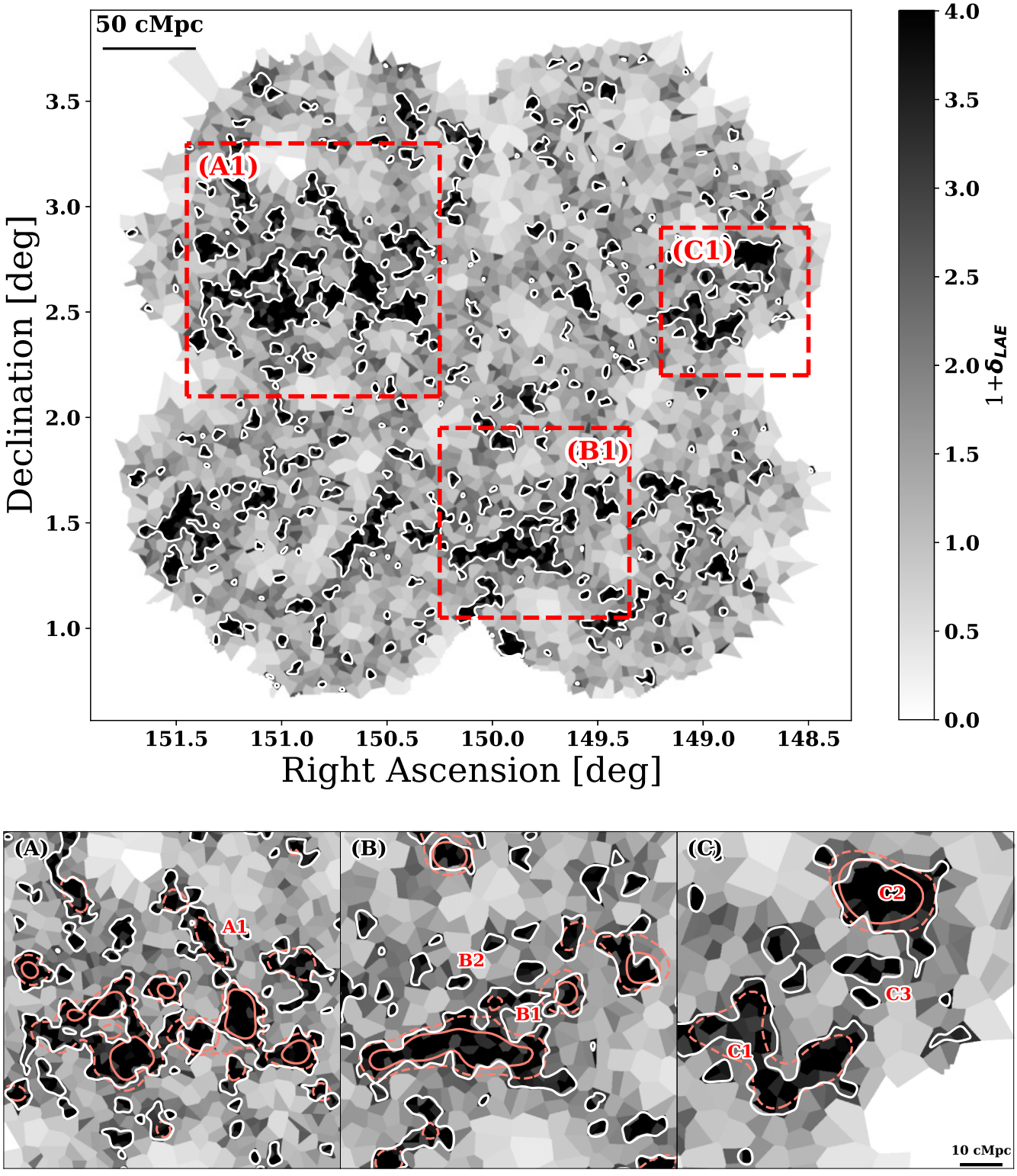

Figure 8. Top: LAE overdensity map constructed from VT (Section 4.2). White lines indicate 3σ overdensity contours. The bottom panels show the three regions—labeled A, B, and C—in the top panel. Overlaid in pink are the 2σ (dashed) and 3σ (solid) contour lines from the GS map. While the GS and VT methods recover similar structures, the latter fares better in detecting anisotropic/intermediate-density structures than the former. Several features of interest are labeled and discussed in the text.

4.4. Cosmic Filaments Traced by LAEs

Our visual examination reveals many linear features connecting extended structures traced by LAEs. Similar features have been observed by spectroscopic surveys in galaxy positions around massive protoclusters (e.g., Cucciati et al. 2018; Huang et al. 2022). Motivated by this, we identify cosmic filaments based on the LAE positions using the Discrete Persistent Structure Extractor code (DisPerSE; Sousbie 2011). Given a set of coordinates, DisPerSE constructs a density map

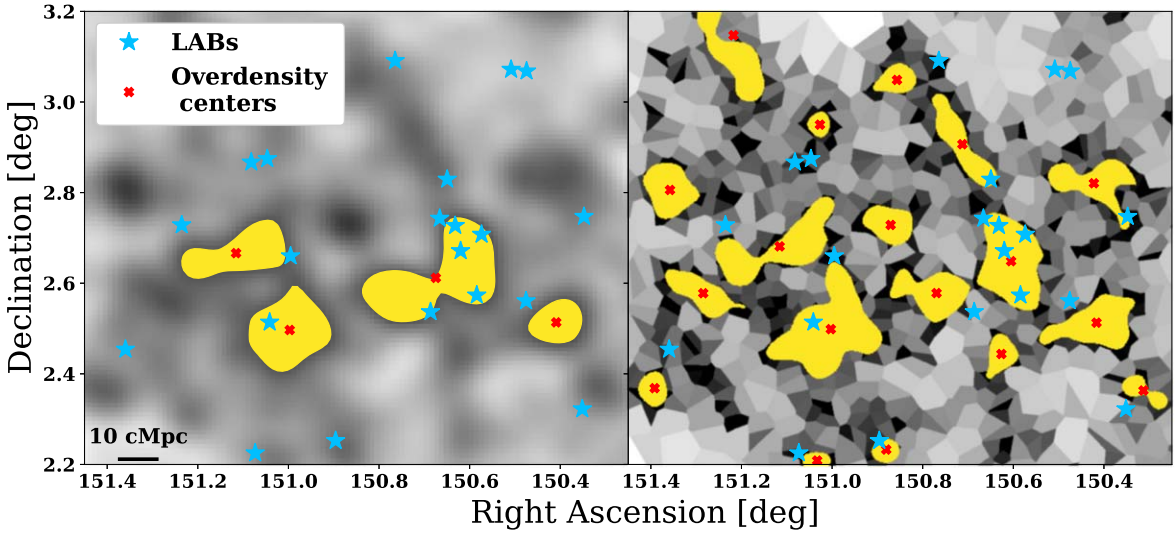

Figure 9. Structures detected in complex A by the GS (left) and VT (right) density maps are shown as yellow swaths. The geometric centers of the structures are marked by red crosses. While both methods identify the most significant structures with a similar angular extent, the VT map fares better in detecting smaller and/or elongated structures and in deblending structures in close proximity. The locations of LABs (blue stars) relative to the detected structures hint at the possible correlation.

based on Delaunay tessellation, and identifies local maxima, minima, and saddle points using the Hessian matrix. Starting from each saddle point, it creates a small segment that runs parallel to the eigenvector of the matrix with a positive eigenvalue. From the end of this segment, the next segment is computed that runs parallel to the gradient vector of the density field. This procedure is repeated until the segments reach a local maximum. Finally, the collection of these segments is extracted as filaments. More details are provided in Sousbie (2011) and Sousbie et al. (2011), while details of the parameters used in this work are given in Appendix B.

In Figure 10, we show the cosmic filaments overlaid with the LAB positions and the VT density map. As expected, the filaments generally follow the distribution of LAEs, tracing the intermediate-density regions that connect adjacent overdensity structures. This is illustrated most clearly in the zoomed-in views of complexes A, B, and C. Each structure is connected to multiple filaments, consistent with the expectations from hierarchical theory. Visual examination suggests a strong relationship between the positions of LABs and filaments, which will be the subject of our discussion in Section 5.3.

5. The Large-scale Environment of LABs

Leveraging the indicators of the large-scale structures identified in Section 4, we explore the environment of LABs in this section. Of the 129 LABs, some lie too close to the image boundaries, and as a result lack robust density estimation. While this is the case for both VT and GS maps, the use of a 10 cMpc Gaussian kernel in the GS map additionally leads to the underestimation of the density within ∼10 cMpc of the edge due to the voids outside it. After removing 27 LABs for these reasons, we use the remaining sample of 102 LABs for the subsequent analyses.

In Figure 11, we show the LAB positions overlaid on the VT map where the white contours highlight the 3σ contours; the 2σ and 3σ contours from the GS map are shown in pink. Visual inspection suggests that LABs preferentially reside in regions of moderate to high density. If LABs are randomly distributed, the expectation is that the mode of $(1+\delta_{\rm LAE})$ at the LAB positions should be 1. Using both the GS and VT maps, we find instead that the mode of $(1+\delta_{\rm LAE})$ is ∼1.5, 1σ away from that expected for a random spatial distribution. This suggests that LABs are not only clustered but prefer higher-density regions.

In Figure 12, we show the number counts of LABs and randomly distributed points as a function of $(1+\delta_{\rm LAE})$ measured in the GS and VT maps. Both are normalized to unity. The Anderson–Darling test rejects the possibility that the two samples are drawn from the same underlying distribution at >99.99% significance. That LABs populate high-density regions traced by LAEs is extremely unlikely to be due to chance alignment.

5.1. Distance of LABs from Protoclusters

To examine the connection between LABs and overdense structures, we calculate the projected distance of each LAB from the center of the nearest protocluster, which we denote as $d_{\rm LAB,PC}$. Similarly, we populate 5000 random points within the field and repeat the same measurements ($d_{\rm rand,PC}$). The result, shown in Figure 13, suggests that the $d_{\rm LAB,PC}$ distribution peaks at a smaller separation than that of $d_{\rm rand,PC}$, i.e., LABs are located closer to protoclusters than warranted by random distribution.

The detailed shape of the distribution is sensitive to our definition of a *protocluster*. In particular, the separation at which the GS and VT estimates peak is very different. The median value is 39 (48) cMpc for LABs (random) in the GS map and 13 (20) cMpc in the VT map. Nevertheless, our results are robust against this variation. The Anderson–Darling test rules out at >99.999% significance that LABs and random points are drawn from the same underlying distribution for both the GS and VT maps. While both methods support the hypothesis that LABs prefer to live close to a protocluster, the relative disparity is noteworthy. As discussed in Section 4.3, the VT map identifies more and smaller structures than the GS map at the same (3σ) significance and fares better in detecting and centroiding structures in close separation. Indeed, we find

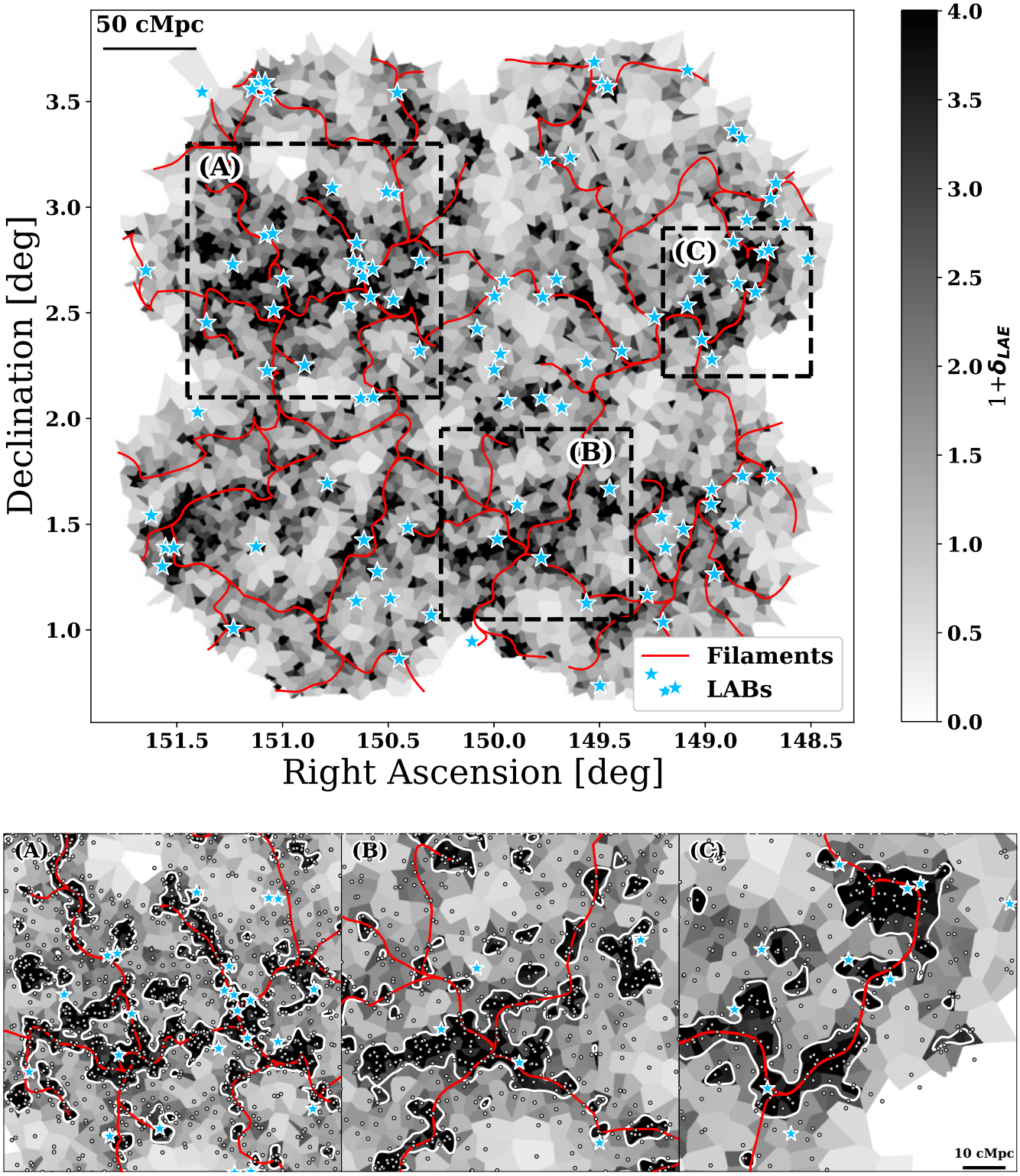

Figure 10. Top: the cosmic filaments traced by LAEs are shown as red lines (see Section 4.4 for more detail); overlaid is the VT map indicating LAE densities in greyscale. The bottom panels show the three regions of interest where the white contours outline the 3σ overdensity levels. Multiple filaments converge on the most significant structures while adjacent structures are connected by filaments. These configurations are in agreement with the expectations from the hierarchical theory of structure formation. The locations of LABs (blue stars) relative to the detected filaments strongly hint at the possibility of a close association.

that ∼26% of the LABs (27 in number) reside inside a structure identified from the VT map. This could be because the GS map often blends multiple overdensity peaks into one and mislocates the centers thereby washing out the trend. Alternatively, LABs could be associated not only with large protoclusters (easily picked up by the GS method) but also with smaller groups, which the VT method is better at identifying. With the larger LAE samples expected from the ODIN survey, we will be able to disentangle the two possibilities in the near future.

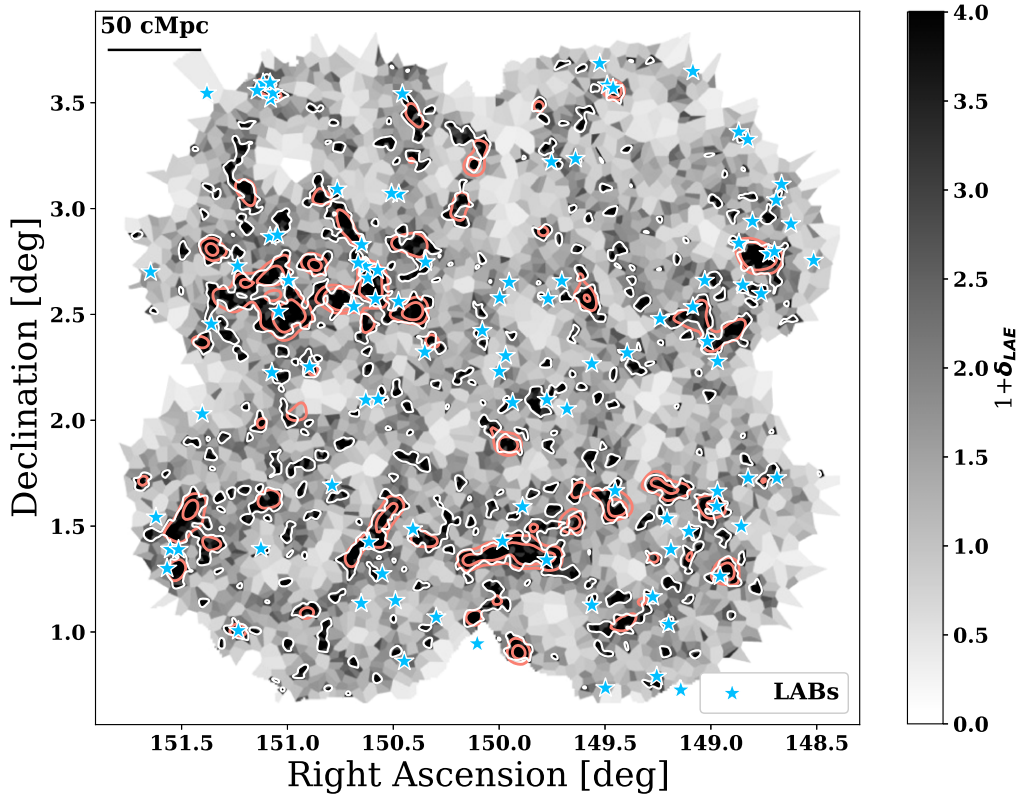

Figure 11. Overdensity map of LAEs in the COSMOS field, constructed from the VT as described in Section 4.2, with the positions of LABs overplotted. Pink contours indicate 2 and 3σ overdensities found in the GS map (Section 4.1), while white contours indicate 3σ overdensities found in the VT map. It is seen that LABs cluster around overdense structures, and seem to occupy regions of high LAE overdensity preferentially.

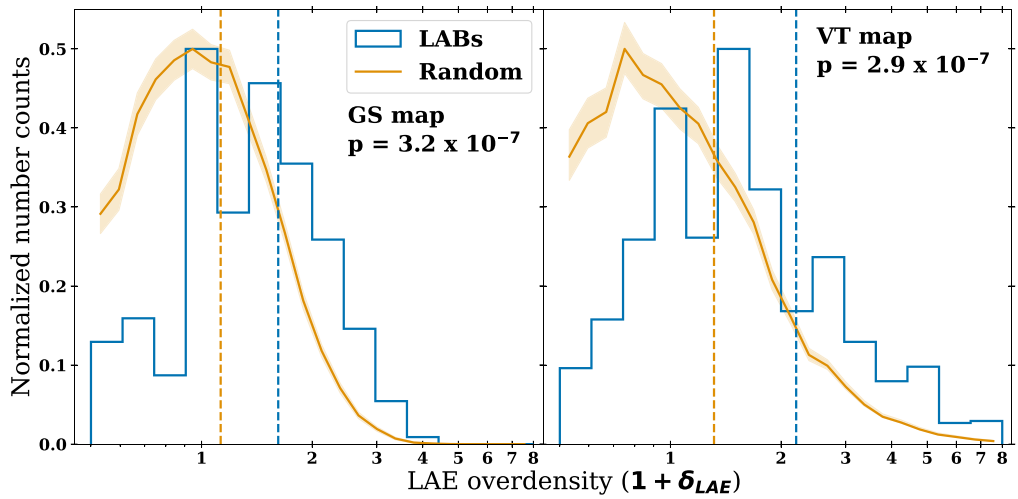

Figure 12. The normalized distribution of LAE density, $(1+\delta_{\rm LAE})$, at the LAB locations (blue) is compared with that of 5000 randomly distributed points (orange) as measured from the GS (left) and VT (right) maps. The shaded orange region shows the spread of the distribution for different realizations of the random points. Blue (orange) dotted lines indicate the median value of the distribution for LABs (random points). The Anderson–Darling test indicates that the probability of the two samples being drawn from the same distribution is of the order 10^{-7}; the p-value for each test is indicated at the right bottom corner.

5.2. LABs and Protocluster Mass

The detection of protoclusters as LAE overdensities allows us to estimate the total mass enclosed therein, which is related to the *present-day mass* of its descendant at $z=0$, $M_{\rm today}$ (Steidel et al. 2000), provided that the bulk of the mass within the overdensity will fall into the center of the potential well. For each protocluster, we estimate the enclosed mass as follows:

$$M_{\rm today} = \sum_i \rho_{m,i} V_{\rm pix} = \sum_i \frac{\delta_{{\rm LAE},i}}{b_{\rm LAE}} \rho_0 V_{\rm pix} = \frac{\rho_0(z)\, V_{\rm pix}}{b_{\rm LAE}} \sum_i \delta_{{\rm LAE},i}, \quad (5)$$

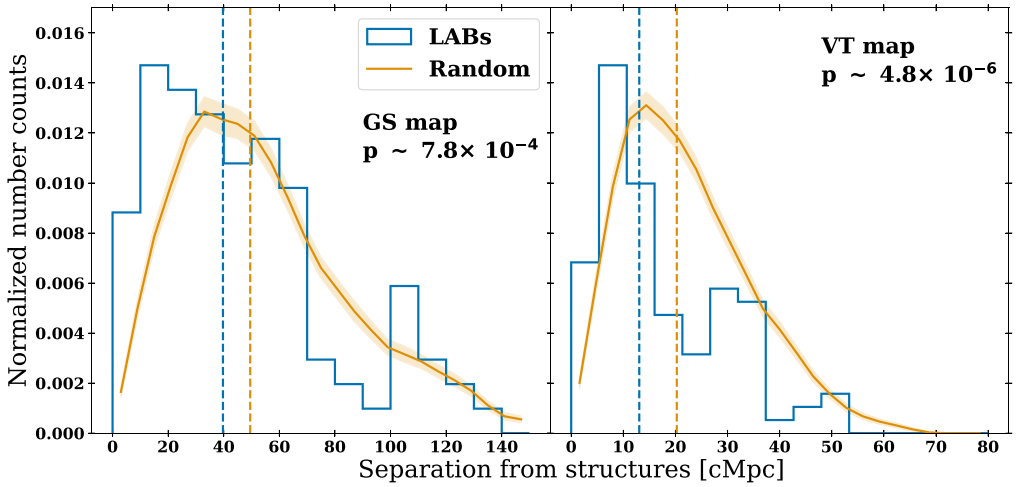

Figure 13. The projected separation of LABs to the nearest overdensity ($d_{\rm LAB,PC}$; blue) is compared with that of random points ($d_{\rm rand,PC}$; orange) where overdensity centers are determined from the GS (left) and VT maps (right). Again the shaded orange region shows the spread of the distribution for different realizations of the random points and blue (orange) dotted lines indicate the median value of the distribution for LABs (random points). In both cases, the two distributions are statistically different in that LABs prefer to reside close to galaxy overdensties.

where $\rho_{m,i}$ and $\delta_{\rm LAE,i}$ are the matter density and the LAE overdensity at pixel i, respectively; $\rho_0(z)$ is the matter density of the universe at $z = 3.1$, $V_{\rm pix}$ is the cosmic volume covered by a single pixel in the VT map, and $b_{\rm LAE}$ is the LAE bias. Each pixel is 120 ckpc on a side, covering 0.015 cMpc^2 in area. We further assume that the extent of each overdensity is comparable in both the line-of-sight and transverse directions, i.e., the cosmic volume spanned by each structure is assumed to be that of a rectangular parallelepiped whose height equals the square root of the angular area. The LAE bias value is fixed at 1.8 (Gawiser et al. 2007).

In this simplistic estimate, $M_{\rm today}$ depends sensitively on the definition of a structure—e.g., the density threshold and the spatial filter size. In addition, changing the bias value within the range found by existing studies (Guaita et al. 2010; Ouchi et al. 2010) leads to ∼20% change in $M_{\rm today}$. However, such changes would largely shift the numerical answers for most protoclusters and therefore should not affect any comparative analyses. We plan to evaluate the validity of the assumptions made here by repeating our analyses on the structures in cosmological hydrodynamic simulations (V. Ramakrishnan et al. 2023, in preparation).

In Figure 14, we show the $M_{\rm today}$ distributions of the protoclusters which host one or more LABs and of those that do not. Evidently, the two are very different; the two-sample Anderson–Darling test differentiates them at >99.99% significance. Protoclusters that host an LAB tend to have much larger $M_{\rm today}$ values than those that do not.

5.3. LABs in the Context of Cosmic Filaments

Motivated by the strong correlation between the LABs and cosmic filaments seen in Figure 10, we explore the physical connection between LABs and the filaments detected by DisPerSE (Section 4.4). A detailed study of the morphologies of ODIN LABs in the context of the LSS will be presented in future work.

We calculate the minimum projected separation of each LAB from the nearest filament, $d_{\rm LAB,fil}$. The same measurements are repeated on a set of 5000 random points, $d_{\rm rand,fil}$. As shown in the left panel of Figure 15, the two distributions are different at

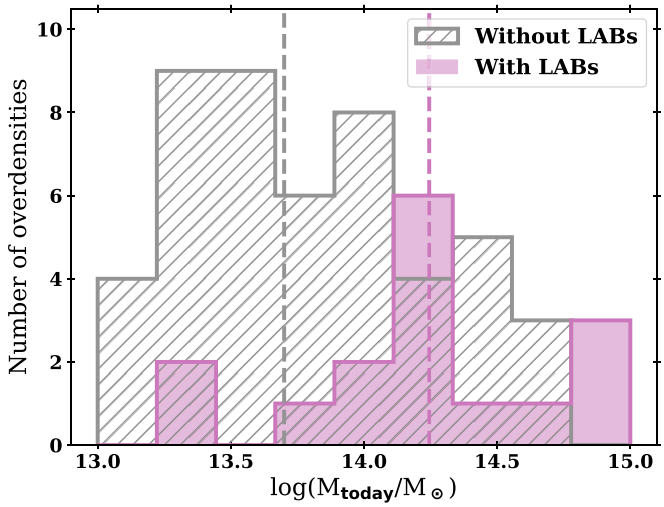

Figure 14. Estimated total masses, $M_{\rm today}$, of protoclusters that host at least one LAB therein (magenta) and those that do not (gray hatched). The median mass (dashed line) of the former is more massive than that of the latter by a factor of ≈3.

>99.99% confidence. The median projected separation is 4.0 (8.2) cMpc for the LABs (random). Of the 102 LABs, 77 (75%) are located within a projected distance of 10 cMpc (2.4 pMpc) from the nearest filament, and 92 (90%) are within 20 cMpc (4.9 pMpc). In comparison, recent hydrodynamic simulations have found that the radius of a filament at $z \sim 3.1$ is ∼2–3 pMpc (Zhu et al. 2021). The significant departure of the $d_{\rm LAB,fil}$ distribution from that of $d_{\rm rand,fil}$ implies that a nonnegligible fraction of the LABs reside inside or close to a filament. Inferring the intrinsic distribution of filament distance from the observed $d_{\rm LAB,fil}$ distribution would require the aid of cosmological simulations and realistic modeling of LAEs therein to account for the projection effect properly, which we will present in future work.

Our results in Section 5.1 show that LABs prefer to live in high-density regions, i.e., near or in protoclusters. Independently, the left panel of Figure 15 demonstrates that the same LABs have the propensity to lie close to filaments. Since

filaments are, by definition, ridges of the density distribution that converge at massive (overdense) structures, it is difficult to understand how these two trends are related and if one is causing the other. To disentangle these effects, we create a set of 100,000 points distributed at random along the length of the DiSPerSE filaments while keeping the distribution of their filament separations matched to those of the LABs.

In the right panel of Figure 15, we show the projected separation from protocluster ($d_{\rm PC}$) of these "random-on-filaments" points and those of the LABs. The p-value returned from the Anderson–Darling test suggests that the two $d_{\rm PC}$ distributions are indistinguishable ($p \sim 0.30$) with similar median values. The implication is that the preference for LABs to reside near or in cosmic web filaments is the primary driver that leads to their proximity to protoclusters; i.e., the latter trend is simply a by-product of the fact that large cosmic structures are where many filaments converge.

However, there exists tentative evidence that filament association may not be the only factor determining where LABs are found. First, LABs are found at slightly higher-density regions than the random-on-filaments points as shown in the middle panel of Figure 15. According to the two-sample Anderson–Darling test, these $(1+\delta_{\rm LAE})$ distributions are different at the ≈98% level. The Komolgorov–Smirnov test returns a consistent result, $p = 0.07$, albeit at lower confidence. This is in qualitative agreement with the trend seen in Figure 14, in that LABs prefer to live in more-massive structures. While these trends are not entirely independent of the observed filament association, it opens up the possibility that LABs may occupy more-evolved regions within filaments and/or have a preferred range of density. In future works, we will leverage larger LAB samples and better characterization of filament detection efficiency to discriminate the different scenarios fully.

5.4. Putting it Together

In this work, we have firmly established that LABs *as a population* prefer to occur in overdense regions and in close proximity to protoclusters and cosmic filaments. Our findings are consistent with the fact that some of the known protoclusters host one or more LABs (e.g., Steidel et al. 2000; Matsuda et al. 2004; Yang et al. 2010, 2011; Prescott et al. 2012; Saito et al. 2015; Caminha et al. 2016; Bădescu et al. 2017; Shi et al. 2019). This could provide some insight into the mechanisms powering LABs—for example, star formation and AGN activity will both be enhanced in overdense regions, which could explain why LABs occur more frequently in these regions. Likewise, in cases where LABs are powered by gravitational cooling (e.g., Daddi et al. 2021), their luminosity would depend on the host halo mass. Studying the relationship between the size and luminosity of LABs and their environment will be useful in addressing this question, and will be done in a future work.

The strong association of LABs with cosmic filaments is not unprecedented. Umehata et al. (2019) detected diffuse mega-parsec-scale Lyα emission from filaments in the SSA22 protocluster and found that two LABs were embedded within these filaments. They speculated that these LABs were regions of enhanced Lyα emission within the otherwise diffuse and faint gas of the filaments. Our results are consistent with this picture. Erb et al. (2011) observed that six LABs at $z = 2.3$ form two linear structures spanning ∼12 Mpc, along which multiple galaxies at the same redshift lie. Given that the morphology of the LABs also appears to be aligned with these linear structures, they speculated that they trace cosmic filaments (see also Kikuta et al. 2019).

Wells et al. (2022) found that galaxies in the vicinity of an LAB are on average brighter, more massive and have a higher star formation rate than those elsewhere, suggesting accelerated galaxy formation around LABs. The energy from the accelerated galaxy formation could then light up the faint gas of the filaments. In this context, the fact that structures that host LABs are likely to have a higher present-day mass than those which do not would be due to the fact that a greater number of filaments converge at more-massive structures. A useful test would be to see if the morphology of LABs is connected with the nearby filaments as observed in Erb et al. (2011) and Kikuta et al. (2019). With the large sample size expected from the full ODIN survey, we will be able to quantify such a relation robustly.

Finally, several existing studies speculated that LABs are likely associated with group-sized halos (e.g., Matsuda et al. 2006; Yang et al. 2010, 2011; Prescott et al. 2015). Bădescu et al. (2017) reasoned that blobs prefer the outskirts of massive structures because they mark the sites of protogroups accreted onto larger protoclusters. The fact that LABs show some evidence of occupying overdense regions even within filaments (Figure 15, middle panel) may be consistent with this hypothesis. With the statistical power afforded by the full ODIN LAB sample, we plan to disentangle the role of filaments, groups, and protoclusters in producing luminous Lyα nebulae, and place more stringent constraints on their formation mechanism.

6. Conclusions

The ODIN survey is currently undertaking deep and wide NB imaging of several extragalactic fields totaling ≈90 deg^2 in area, with the primary aim of identifying Lyα-emitting sources at $z = 2.4$, 3.1, and 4.5. In this work, we have used the early ODIN science data covering ∼10 deg^2 in the extended COSMOS field and identified a sample of 5352 LAEs and 129 LABs at $z = 3.1$ in the largest contiguous cosmic volume to date spanning ≈350 × 350 × 70 (cMpc)^3. Using these data, we investigate how LABs are connected to their large-scale environment as traced by LAEs. Our main conclusions are:

1. Using the LAE population as a tracer of the underlying matter distribution, we have identified overdense structures as galaxy groups, protoclusters, and filaments of the cosmic web. We find that protoclusters and smaller groups are often strongly clustered together and form extended complexes. The morphologies of these structures are highly irregular and nonspherical; the largest systems are connected to multiple filaments which connect them to smaller structures. These observations are in accordance with expectations from hierarchical structure formation.

2. We find that LABs preferentially reside in high-density regions. When compared to randomly located points in the same field, the $(1+\delta_{\rm LAE})$ distribution of the LABs shows a clear excess and a deficit at the high- and low-density ends, respectively. The two distributions are dissimilar at an extremely high statistical significance, suggesting that our finding is unlikely to be due to chance alignment.

3. Starting from the LAE density maps constructed using Gaussian fixed-kernel smoothing (GS map) and Voronoi

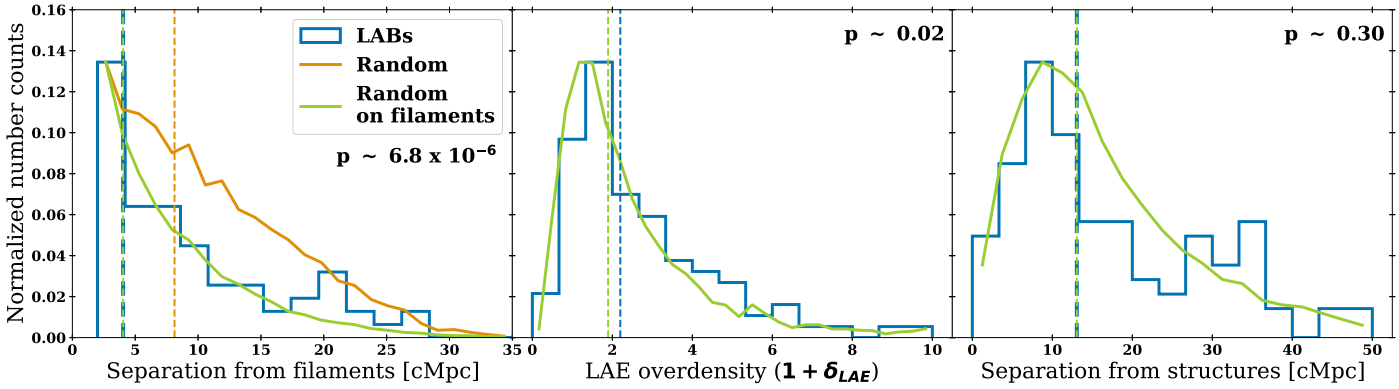

Figure 15. The minimum separation from filaments ($d_{\rm fil}$, left), LAE density ($1+\delta_{\rm LAE}$, middle), and minimum separation from a protocluster ($d_{\rm PC}$, right) distributions of LABs (blue), random (orange), and random-on-filament points (green). The p-value indicated at the top right corner of each panel is from the two-sample Anderson–Darling test. The filament distances of LABs, $d_{\rm LAB,fil}$, are strongly skewed toward low values relative to a 2D random distribution. When a set of random-on-filaments points that match the $d_{\rm LAB,fil}$ distribution is used as a control sample, the LAB distribution of the minimum distance to protoclusters, $d_{\rm PC}$, is naturally reproduced. The implication is that the primary association of LABs is to filaments and not to protoclusters.

tessellation (VT map), we explore ways to detect cosmic structures, which we broadly refer to as protoclusters. Due to the irregular and often linear/filamentary nature of the angular distribution of the LAEs, we determine that the VT map performs better at detecting protoclusters and at separating them when two are adjacent but distinct. Regardless of the detection method, LABs tend to be located in or near groups and protoclusters, with ≈30% of the LABs residing within a structure. Additionally, we find that protoclusters hosting one or more LABs tend to have larger descendant (today) masses than those that do not.

4. LABs are also strongly correlated with cosmic filaments. Of our LABs, ≈70% (85) are found within a projected filament distance corresponding to 2.4 pMpc. Given that the radius of a filament at $z=3.1$ is expected to be 2–3 pMpc, our result suggests that a nonnegligible fraction of the LABs reside inside or close to a filament. Inferring the intrinsic distribution of the separation of LABs from cosmic filaments requires the aid of cosmological simulations and realistic modeling of galaxies therein, which we will investigate with the larger samples expected from the ODIN survey.

5. The strong association of the LABs to protoclusters and to filaments is connected. When we generate a set of "random-on-filaments" points that match the distribution of the projected filament distanced of the LABs ($d_{\rm fil}$), the distribution of the minimum separations from a protocluster ($d_{\rm PC}$) measured for the LAB sample is naturally reproduced. The implication is that the preference of an LAB to reside near or in cosmic web filaments is the primary driver that leads to their proximity to protoclusters because large cosmic structures are where many filaments converge.

Acknowledgments

Based on observations at Cerro Tololo Inter-American Observatory, NSF's NOIRLab (Prop. ID 2020B-0201; PI: K.-S. Lee), which is managed by the Association of Universities for Research in Astronomy under a cooperative agreement with the National Science Foundation. The authors acknowledge financial support from the National Science Foundation under grant Nos. AST-2206705 and AST-2206222 and from the Ross-Lynn Purdue Research Foundation Grant. B.M. and Y.Y. are supported by the Basic Science Research Program through the National Research Foundation of Korea funded by the Ministry of Science, ICT & Future Planning (2019R1A2C4069803). This work was supported by K-GMT Science Program (GEMINI-KR-2021B-008) of Korea Astronomy and Space Science Institute. The Institute for Gravitation and the Cosmos is supported by the Eberly College of Science and the office of the Senior Vice President for Research at the Pennsylvania State University. A.I.Z. acknowledges support from NSF AST-1715609 and thanks the hospitality of the Columbia Astrophysics Laboratory at Columbia University where some of this work was completed. M.C.A. acknowledges financial support from the Seal of Excellence @UNIPD 2020 program under the ACROGAL project.

Facilities: Blanco (DECam), Gemini:South (GMOS)

Appendix A
Comparing Blobs to the General Galaxy Population

In Section 5, we demonstrate that LABs live in regions of high LAE density, $(1+\delta_{\rm LAE})$, compared to those of random points. A more pertinent question may be: where are LABs found relative to the general galaxy population? While obtaining a clear answer to this question requires deep wide-field spectroscopy and is thus costly, it would tell us more directly about the relationship between LABs and protoclusters and about the preferred range of environmental density or halo mass in which LABs reside. Alternatively, we can use LAEs as a representative subset of the underlying galaxy population.

In Figure 16, we plot the cumulative $(1+\delta_{\rm LAE})$ distribution of LAEs and LABs. The two are nearly identical, as can be seen visually and confirmed by the Anderson–Darling test. Taken at face value, our result suggests that LAEs and LABs intrinsically occupy the same environments; this may seem surprising and even contradictory to our finding that LABs prefer to be near protoclusters and are expected to have a higher galaxy bias. Another possibility is that the two have different distributions but the present data are insufficient to distinguish them as such.

We quantify the discriminating power of our data set by running a test using the IllustrisTNG simulation to address the following question: if LABs reside in more-massive halos than LAEs, how well would we be able to detect the trend? To this end, we use the $z=3$ snapshot of the TNG 300 cMpc box and cut out a 60 cMpc slice along the x-, y-, or z-direction to match the $N501$ filter width. The transverse size of the TNG300 box is

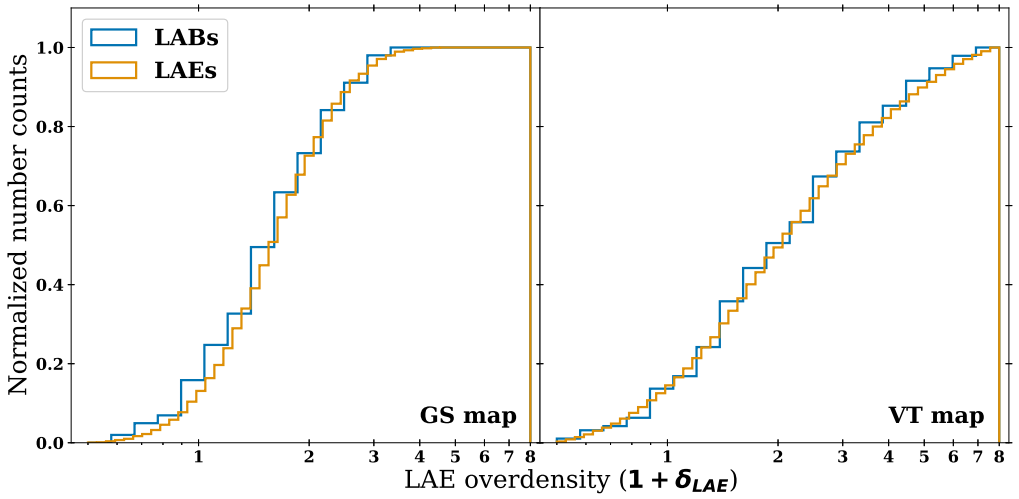

Figure 16. The cumulative distribution of the $(1+\delta_{\rm LAE})$ on the positions of LAEs (orange) and LABs (blue) where the LAE density is measured using the GS (left) and VT (right) methods. The two distributions are statistically similar and cannot be distinguished by the Anderson–Darling test.

Table 2
Surface density distributions of LAEs vs LABs.

	$M_{\rm min,LAE}=10^9\,M_\odot$			$M_{\rm min,LAE}=10^{10}\,M_\odot$			$M_{\rm min,LAE}=10^{11}\,M_\odot$		
	$p_{\rm min}$	$p_{\rm max}$	$f_{p<0.05}$	$p_{\rm min}$	$p_{\rm max}$	$f_{p<0.05}$	$p_{\rm min}$	$p_{\rm max}$	$f_{p<0.05}$
				ODIN COSMOS					
GS map	6.6×10^{-5}	1.0	0.17	8.4×10^{-5}	1.0	0.16	1.2×10^{-5}	1.0	0.22
VT map	3.4×10^{-5}	1.0	0.17	3.3×10^{-5}	1.0	0.17	1.7×10^{-5}	1.0	0.21
				ODIN Full					
GS map	5.6×10^{-7}	0.77	0.81	5.6×10^{-6}	0.88	0.79	2.9×10^{-7}	0.36	0.98
VT map	1.8×10^{-6}	0.77	0.61	1.3×10^{-5}	0.93	0.60	2.2×10^{-6}	0.80	0.74

Notes. Comparison of the $(1+\delta_{\rm LAE})$ distributions of mock "LAEs" and "LABs" selected in IllustrisTNG using the Anderson–Darling test. Mock LAEs are assigned to a random subset of halos with masses $> M_{\rm min,LAE}$. We fix $M_{\rm min,LAB}$ to $10^{12}\,M_\odot$. The minimum/maximum p-values and the fraction in which the two distributions are different at >95% level ($f_{p<0.05}$) are based on 1000 realizations.

well matched to our survey field ($7.5\,{\rm deg}^2 \approx 9.9\times10^4$ cMpc^2 at $z=3.1$ compared to 9.0×10^4 cMpc^2 in TNG300). In this volume, we randomly pick dark matter halos above a given mass threshold $M_{\rm min,LAE}$ and assign them as "LAEs." Similarly, "LABs" are a random subset of the halos above $M_{\rm min,LAB}$, which is set to $10^{12}\,M_\odot$. The latter assumption is made based on clustering measurements (B. Moon et al. 2023, in preparation). The surface densities of these mock LAEs and LABs are matched to those observed in our data.

Using these mock LAE and LAB samples, we repeat the same steps taken in Sections 4.1 and 4.2 and measure the $(1+\delta_{\rm LAE})$ distributions. This procedure is repeated 1000 times each time reselecting a $300\times300\times60$ (cMpc)^3 subsection of the TNG volume and reassigning LABs and LAEs to a subset of halos therein. In Table 2, we list the minimum and maximum p-values returned by the Anderson–Darling test in these realizations ($p_{\rm min}$ and $p_{\rm max}$) and the fraction in which the two distributions are distinguishable at >95% significance ($f_{p<0.05}$). We try three $M_{\rm min,LAE}$ values, $10^9\,M_\odot$, $10^{10}\,M_\odot$, and $10^{11}\,M_\odot$. While we do not vary $M_{\rm min,LAB}$, the expectation is that lower $M_{\rm min,LAB}$ values would mean that LABs have galaxy biases more similar to LAEs, making it more difficult to discriminate the distributions. The true $M_{\rm min,LAB}$ value is unlikely to be greater than $10^{12}\,M_\odot$. If all halos with masses $M\geqslant10^{12}\,M_\odot$ host an LAB, the LAB surface density would be comparable to that observed in our data.

From the table, only in 17%–22% of the realizations are the two distributions meaningfully different regardless of the minimum halo mass assigned to the LAEs. In light of this, it is not surprising that we are unable to distinguish the two distributions in the real data given the current sample size. We take a step further and forecast how well our measurements will improve once the full ODIN data set at $z=3.1$ is at hand, which will be nine times larger than the current data set. The result is shown in the bottom half of Table 2. The fraction in which the two distributions are distinguishable, $f_{p<0.05}$, is significantly higher at 74%–98%. However, the range of p-values remains wide, implying that it is not a guaranteed outcome.

The observed large statistical uncertainty is in part due to small number statistics for LABs combined with the high cosmic variance expected for massive halos hosting them. In addition, we remind readers of another caveat. Since LAEs themselves are used to compute the overdensity, the high end of the $(1+\delta_{\rm LAE})$ distribution for LAEs is bound to be overrepresented compared to any other galaxy sample. For example, if one "pixel" in the density map contains six LAEs therein, we would count that pixel six times instead of one. A more equitable comparison may be made using galaxy samples identified regardless of their Lyα emission, e.g., a stellar-mass- or $M_{\rm UV}$-limited sample. With ≈1000 LABs at each redshift ($z=2.4$, 3.1, and 4.5) expected at the completion of the ODIN

survey, measurement of angular clustering to infer their host halo masses remains a viable alternative.

Appendix B
Filaments of the Cosmic Web with Different Detection Settings

In running DisPerSE, we use the `-btype smooth` option, which generates additional points outside the field boundaries via interpolation intended to mitigate the edge effect. The choice of persistence is important as a higher persistence setting extracts more-robust but less-detailed filamentary structures. We set persistence to 2.5σ, slightly lower than those used in recent studies (e.g., Malavasi et al. 2016; Kraljic et al. 2017). In the left panel of Figure 17, we show the filaments identified using persistence set to 2.5σ and 3σ. While most of the filaments in the regions of interest (e.g., complexes A, B, and C) are detected with both persistence values, one long structure in complex A is undetected when persistence is set to 3σ. Since the same region also shows an excess of LABs (see the bottom panel (A) in Figure 10), we set it to 2.5σ for our final set of filaments.

We also test how the regions excluded by bright star masks affect our ability to identify filaments meaningfully. This is done by filling in the masked regions with a random set of points commensurate with the field LAE density. The result is shown in the right panel of Figure 17. While the two sets of filaments are not identical, only the shortest filaments tend to be significantly affected. The majority of the filaments are left unchanged. Using either set of filaments does not change our main conclusions.

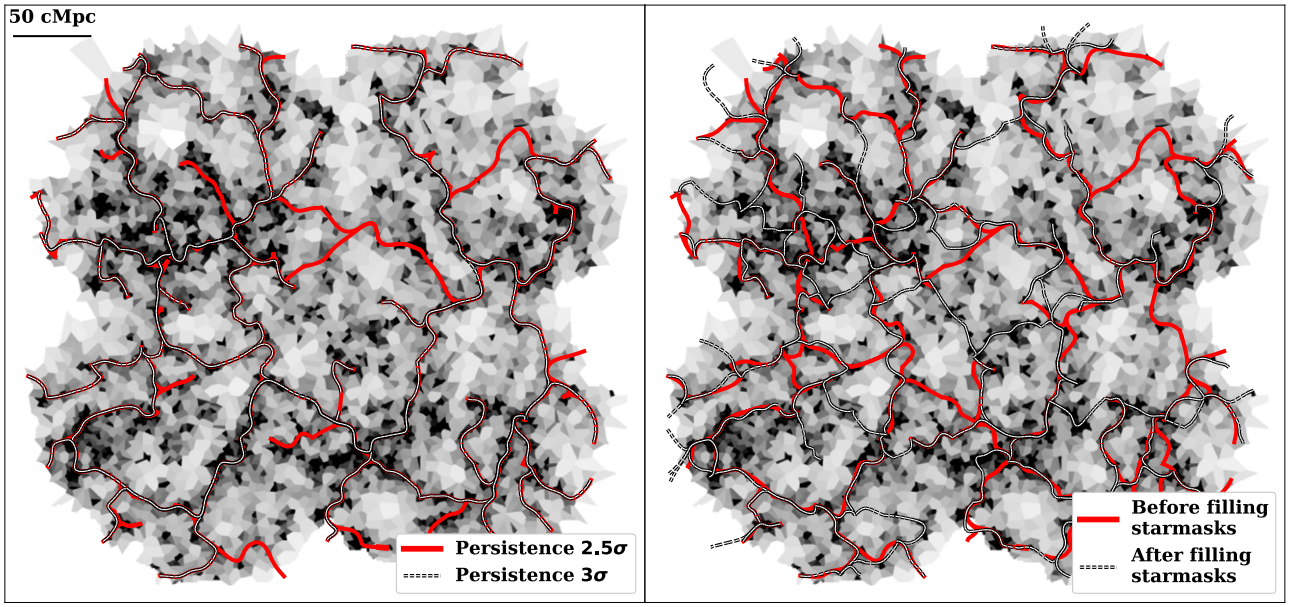

Figure 17. DisPerSE-detected filaments are shown as red and white segments when we change the persistence level (left) and fill in the regions of bright stars with random points (right). The background in both panels is the VT-based $(1 + \delta_{\rm LAE})$ density map. While the number of filaments depends on the run setting, a majority of filaments in and around the densest regions are detected in both. Our main conclusions remain robust against these changes.

ORCID iDs

Vandana Ramakrishnan https://orcid.org/0000-0002-9176-7252
Kyoung-Soo Lee https://orcid.org/0000-0003-3004-9596
Eric Gawiser https://orcid.org/0000-0003-1530-8713
Yujin Yang https://orcid.org/0000-0003-3078-2763
Changbom Park https://orcid.org/0000-0001-9521-6397
Ho Seong Hwang https://orcid.org/0000-0003-3428-7612
Francisco Valdes https://orcid.org/0000-0001-5567-1301
Maria Celeste Artale https://orcid.org/0000-0003-0570-785X
Robin Ciardullo https://orcid.org/0000-0002-1328-0211
Arjun Dey https://orcid.org/0000-0002-4928-4003
Caryl Gronwall https://orcid.org/0000-0001-6842-2371
Lucia Guaita https://orcid.org/0000-0002-4902-0075
Woong-Seob Jeong https://orcid.org/0000-0002-2770-808X
Nelson Padilla https://orcid.org/0000-0001-9850-9419
Akriti Singh https://orcid.org/0009-0000-7651-3900
Ann Zabludoff https://orcid.org/0000-0001-6047-8469

References

Aihara, H., Arimoto, N., Armstrong, R., et al. 2018a, PASJ, 70, S4
Aihara, H., AlSayyad, Y., Ando, M., et al. 2019, PASJ, 71, 114
Aihara, H., Armstrong, R., Bickerton, S., et al. 2018b, PASJ, 70, S8
Alberts, S., Pope, A., Brodwin, M., et al. 2014, MNRAS, 437, 437
Alberts, S., Pope, A., Brodwin, M., et al. 2016, ApJ, 825, 72
Ao, Y., Matsuda, Y., Henkel, C., et al. 2017, ApJ, 850, 178
Araya-Araya, P., Vicentin, M. C., & Sodré 2021, MNRAS, 504, 5054
Arrigoni Battaia, F., Chen, C.-C., Liu, H.-Y. B., et al. 2022, ApJ, 930, 72
Barbary, K. 2016, JOSS, 1, 58
Bernstein, G. M., Abbott, T. M. C., Desai, S., et al. 2017, PASP, 129, 114502
Bertin, E. 2006, in ASP Conf. Ser. 351, Astronomical Data Analysis Software and Systems XV, ed. C. Gabriel et al. (San Francisco, CA: ASP), 112
Bertin, E., & Arnouts, S. 1996, A&AS, 117, 393
Boylan-Kolchin, M., Springel, V., White, S. D. M., Jenkins, A., & Lemson, G. 2009, MNRAS, 398, 1150
Bădescu, T., Yang, Y., Bertoldi, F., et al. 2017, ApJ, 845, 172
Cai, Z., Fan, X., Yang, Y., et al. 2017, ApJ, 837, 71
Caminha, G. B., Karman, W., Rosati, P., et al. 2016, A&A, 595, A100
Casey, C. M., Cooray, A., Capak, P., et al. 2015, ApJL, 808, L33
Chang, S.-J., Yang, Y., Seon, K.-I., Zabludoff, A., & Lee, H.-W. 2023, ApJ, 945, 100
Chiang, Y.-K., Overzier, R., & Gebhardt, K. 2013, ApJ, 779, 127
Chiang, Y.-K., Overzier, R., & Gebhardt, K. 2014, ApJL, 782, L3
Ciardullo, R., Gronwall, C., Wolf, C., et al. 2012, ApJ, 744, 110
Coupon, J., Czakon, N., Bosch, J., et al. 2018, PASJ, 70, S7
Cucciati, O., Lemaux, B. C., Zamorani, G., et al. 2018, A&A, 619, A49
Daddi, E., Valentino, F., Rich, R. M., et al. 2021, A&A, 649, A78
Darvish, B., Mobasher, B., Sobral, D., Scoville, N., & Aragon-Calvo, M. 2015, ApJ, 805, 121
Darvish, B., Scoville, N. Z., Martin, C., et al. 2020, ApJ, 892, 8
Davis, M., Efstathiou, G., Frenk, C. S., & White, S. D. M. 1985, ApJ, 292, 371
Dey, A., Bian, C., Soifer, B. T., et al. 2005, ApJ, 629, 654
Dey, A., Lee, K.-S., Reddy, N., et al. 2016, ApJ, 823, 11
Dijkstra, M., & Wyithe, J. S. B. 2012, MNRAS, 419, 3181
Elbaz, D., Daddi, E., Le Borgne, D., et al. 2007, A&A, 468, 33
Erb, D. K., Bogosavljević, M., & Steidel, C. C. 2011, ApJL, 740, L31
Fardal, M. A., Katz, N., Gardner, J. P., et al. 2001, ApJ, 562, 605
Flaugher, B., Diehl, H. T., Honscheid, K., et al. 2015, AJ, 150, 150
Francis, P. J., Woodgate, B. E., Warren, S. J., et al. 1996, ApJ, 457, 490
Gaia Collaboration, Brown, A. G. A., Vallenari, A., et al. 2021, A&A, 649, A1
Gawiser, E., Francke, H., Lai, K., et al. 2007, ApJ, 671, 278
Gawiser, E., van Dokkum, P. G., Gronwall, C., et al. 2006a, ApJL, 642, L13
Gawiser, E., van Dokkum, P. G., Herrera, D., et al. 2006b, ApJS, 162, 1
Geach, J. E., Alexander, D. M., Lehmer, B. D., et al. 2009, ApJ, 700, 1
Geach, J. E., Narayanan, D., Matsuda, Y., et al. 2016, ApJ, 832, 37
Gronwall, C., Ciardullo, R., Hickey, T., et al. 2007, ApJ, 667, 79
Guaita, L., Acquaviva, V., Padilla, N., et al. 2011, ApJ, 733, 114
Guaita, L., Gawiser, E., Padilla, N., et al. 2010, ApJ, 714, 255
Harikane, Y., Ouchi, M., Ono, Y., et al. 2019, ApJ, 883, 142
Hayashi, M., Kodama, T., Tadaki, K.-i., Koyama, Y., & Tanaka, I. 2012, ApJ, 757, 15
Hayes, M., Scarlata, C., & Siana, B. 2011, Natur, 476, 304
Hibon, P., Tang, F., & Thomas, R. 2020, A&A, 641, A32
Higuchi, R., Ouchi, M., Ono, Y., et al. 2019, ApJ, 879, 28
Hong, S., Dey, A., Lee, K.-S., et al. 2019, MNRAS, 483, 3950
Huang, Y., Lee, K.-S., Cucciati, O., et al. 2022, ApJ, 941, 134
Hung, D., Lemaux, B. C., Gal, R. R., et al. 2020, MNRAS, 491, 5524
Hwang, H. S., Shin, J., & Song, H. 2019, MNRAS, 489, 339
Jiang, L., Wu, J., Bian, F., et al. 2018, NatAs, 2, 962
Kaiser, N. 1984, ApJL, 284, L9
Kawinwanichakij, L., Papovich, C., Quadri, R. F., et al. 2017, ApJ, 847, 134
Khostovan, A. A., Sobral, D., Mobasher, B., et al. 2019, MNRAS, 489, 555
Kikuta, S., Matsuda, Y., Cen, R., et al. 2019, PASJ, 71, L2
Kim, E., Yang, Y., Zabludoff, A., et al. 2020, ApJ, 894, 33
Komatsu, E., Smith, K. M., Dunkley, J., et al. 2011, ApJS, 192, 18
Koyama, Y., Polletta, M. d. C., Tanaka, I., et al. 2021, MNRAS Lett., 503, L1
Kraljic, K., Arnouts, S., Pichon, C., et al. 2017, MNRAS, 474, 547
Kuchner, U., Haggar, R., Aragón-Salamanca, A., et al. 2022, MNRAS, 510, 581
Lee, K.-S., Dey, A., Hong, S., et al. 2014, ApJ, 796, 126
Lemaux, B. C., Cucciati, O., Le Fèvre, O., et al. 2022, A&A, 662, A33
Lemaux, B. C., Le Fèvre, O., Cucciati, O., et al. 2018, A&A, 615, A77
Malavasi, N., Arnouts, S., Vibert, D., et al. 2016, MNRAS, 465, 3817
Malavasi, N., Lee, K.-S., Dey, A., et al. 2021, ApJ, 921, 103
Malhotra, S., Rhoads, J. E., Finkelstein, S. L., et al. 2012, ApJL, 750, L36
Matsuda, Y., Yamada, T., Hayashino, T., et al. 2004, AJ, 128, 569
Matsuda, Y., Yamada, T., Hayashino, T., et al. 2011, MNRAS Lett., 410, L13
Matsuda, Y., Yamada, T., Hayashino, T., Yamauchi, R., & Nakamura, Y. 2006, ApJL, 640, L123
Momose, R., Shimasaku, K., Kashikawa, N., et al. 2021, ApJ, 909, 117
Nantais, J. B., van der Burg, R. F. J., Lidman, C., et al. 2016, A&A, 592, A161
Nelson, D., Springel, V., Pillepich, A., et al. 2019, ComAC, 6, 2
Norberg, P., Baugh, C. M., Hawkins, E., et al. 2002, MNRAS, 332, 827
Oke, J. B., & Gunn, J. E. 1983, ApJ, 266, 713
Oteo, I., Ivison, R. J., Dunne, L., et al. 2018, ApJ, 856, 72
Ouchi, M., Ono, Y., & Shibuya, T. 2020, ARA&A, 58, 617
Ouchi, M., Shimasaku, K., Furusawa, H., et al. 2010, ApJ, 723, 869
Overzier, R. A. 2016, A&ARv, 24, 14
Paulino-Afonso, A., Sobral, D., Ribeiro, B., et al. 2018, MNRAS, 476, 5479
Peng, Y.-j., Lilly, S. J., Kovač, K., et al. 2010, ApJ, 721, 193
Pillepich, A., Nelson, D., Hernquist, L., et al. 2018b, MNRAS, 475, 648
Pillepich, A., Springel, V., Nelson, D., et al. 2018a, MNRAS, 473, 4077
Planck Collaboration, Ade, P. A. R., Aghanim, N., et al. 2016, A&A, 594, A13
Prescott, M. K. M., Dey, A., Brodwin, M., et al. 2012, ApJ, 752, 86
Prescott, M. K. M., Kashikawa, N., Dey, A., & Matsuda, Y. 2008, ApJL, 678, L77
Prescott, M. K. M., Momcheva, I., Brammer, G. B., Fynbo, J. P. U., & Møller, P. 2015, ApJ, 802, 32
Quadri, R. F., Williams, R. J., Franx, M., & Hildebrandt, H. 2012, ApJ, 744, 88
Rosdahl, J., & Blaizot, J. 2012, MNRAS, 423, 344
Saito, T., Matsuda, Y., Lacey, C. G., et al. 2015, MNRAS, 447, 3069
Sarron, F., & Conselice, C. J. 2021, MNRAS, 506, 2136
Schlafly, E. F., Finkbeiner, D. P., Jurić, M., et al. 2012, ApJ, 756, 158
Shi, K., Huang, Y., Lee, K.-S., et al. 2019, ApJ, 879, 9
Shi, K., Toshikawa, J., Cai, Z., Lee, K.-S., & Fang, T. 2020, ApJ, 899, 79
Shimakawa, R., Kodama, T., Hayashi, M., et al. 2017, MNRAS Lett., 468, L21
Sousbie, T. 2011, MNRAS, 414, 350
Sousbie, T., Pichon, C., & Kawahara, H. 2011, MNRAS, 414, 384
Steidel, C. C., Adelberger, K. L., Shapley, A. E., et al. 2000, ApJ, 532, 170
Taniguchi, Y., & Shioya, Y. 2000, ApJL, 532, L13
Toshikawa, J., Kashikawa, N., Overzier, R., et al. 2016, ApJ, 826, 114
Toshikawa, J., Uchiyama, H., Kashikawa, N., et al. 2018, PASJ, 70, S12
Umehata, H., Fumagalli, M., Smail, I., et al. 2019, Sci, 366, 97
Umehata, H., Tamura, Y., Kohno, K., et al. 2015, ApJL, 815, L8
Valdes, F. 2021, The DECam Community Pipeline Instrumental Signature Removal, https://legacy.noirlab.edu/noao/staff/fvaldes/Pipelines/Docs/PL206/
Valdes, F., & Gruendl, R. 2014, in ASP Conf. Ser. 485, ed. N. Manset & P. Forshay (San Francisco, CA: ASP), 379
van der Burg, R. F. J., Muzzin, A., Hoekstra, H., et al. 2013, A&A, 557, A15
Vogelsberger, M., Nelson, D., Pillepich, A., et al. 2020, MNRAS, 492, 5167
Weinberger, L. H., Haehnelt, M. G., & Kulkarni, G. 2019, MNRAS, 485, 1350

Wells, N. K., Prescott, M. K. M., & Finlator, K. M. 2022, ApJ, 941, 180
Yang, Y., Walter, F., Decarli, R., et al. 2014a, ApJ, 784, 171
Yang, Y., Zabludoff, A., Eisenstein, D., & Davé, R. 2010, ApJ, 719, 1654
Yang, Y., Zabludoff, A., Jahnke, K., et al. 2011, ApJ, 735, 87
Yang, Y., Zabludoff, A., Jahnke, K., & Davé, R. 2014b, ApJ, 793, 114
Yang, Y., Zabludoff, A., Tremonti, C., Eisenstein, D., & Davé, R. 2009, ApJ, 693, 1579
You, C., Zabludoff, A., Smith, P., et al. 2017, ApJ, 834, 182
Zheng, X. Z., Cai, Z., An, F. X., Fan, X., & Shi, D. D. 2021, MNRAS, 500, 4354
Zhu, W., Zhang, F., & Feng, L.-L. 2021, ApJ, 920, 2